Research Square

Preprints are preliminary reports that have not undergone peer review.
They should not be considered conclusive, used to inform clinical practice,
or referenced by the media as validated information.

Biophysical Feasibility Constraints Govern Phase Transitions in Tumor Control Dynamics

Enrique Rosario Aloma

erosarioaloma@barry.edu

Barry University

Luis Rodriguez

Barry University

Carolina Vigo

Barry University

Maymunah Ray

Barry University

Rolando Petit

Barry University

Article

Keywords: Nonlinear dynamical systems, Bifurcation structure, Phase transitions, Reaction–diffusion systems, Multistability, Environmental coupling, Stability analysis, Dimensionless control parameters, Transport-limited dynamics, Energetic constraints

Posted Date: February 27th, 2026

DOI: https://doi.org/10.21203/rs.3.rs-8959124/v1

License: This work is licensed under a Creative Commons Attribution 4.0 International License.
Read Full License

Additional Declarations: No competing interests reported.

Biophysical Feasibility Constraints Govern Phase Transitions in Tumor Control Dynamics

Authors:

1. Enrique Rosario Aloma
   College of Health Professions and Medical Sciences
   Barry University
   City: Miami State: Florida Country: United States
   Email: erosarioaloma@barry.edu
   ORCID: 0000-0003-3069-1124
   Corresponding Author

2. Luis Rodriguez
   College of Health Professions and Medical Sciences
   Barry University
   City: Miami State: Florida Country: United States
   Email: larodriguez@barry.edu

3. Carolina Vigo
   College of Health Professions and Medical Sciences
   Barry University
   City: Miami State: Florida Country: United States
   Email: cvigo@barry.edu

4. Maymunah Ray
   College of Health Professions and Medical Sciences
   Barry University
   City: Miami State: Florida Country: United States
   Email: mray@barry.edu

5. Rolando Petit
   College of Health Professions and Medical Sciences
   Barry University
   City: Miami State: Florida Country: United States
   Email: rpetit@barry.edu

ABSTRACT

Tumor behavior is strongly influenced by microenvironmental acidity, molecular transport, and metabolic resource limitations, yet quantitative principles governing their coupled effects remain incompletely understood. Here we present a biophysical modeling framework showing that sustained tumor control is governed by feasibility constraints rather than by individual parameter magnitudes. Three dimensionless control parameters (Ξ, Λ, Ψ) capture independent dynamical, spatial, and energetic limitations arising from nonlinear tumor–immune interactions, reaction–diffusion transport of acidity, and metabolic costs of alkalinization. Analytical feasibility boundaries defined by these parameters predict distinct outcome regimes, including tumor persistence, partial control, and clearance. Numerical parameter sweeps reveal sharp transitions across feasibility thresholds, and sensitivity analysis demonstrates that regime structure depends primarily on the dimensionless constraint geometry rather than on specific kinetic coefficients. These results introduce a constraint-based interpretation of tumor regulation and clarify how transport and energetic limitations can fundamentally restrict therapeutic outcomes. The framework provides a generalizable approach for analyzing environmentally coupled biological systems subject to physical constraints.

Keywords

Nonlinear dynamical systems
Bifurcation structure
Phase transitions
Reaction–diffusion systems
Multistability
Environmental coupling
Stability analysis
Dimensionless control parameters
Transport-limited dynamics
Energetic constraints

1. INTRODUCTION

Many physical, biological, and engineered systems operate under conditions in which the governing dynamics are inseparably coupled to a regulatory environment that is itself dynamically modified by the system's state. Such environmentally coupled systems exhibit behaviors that cannot be fully understood through isolated kinetic models, as feedback between agents and environmental fields introduces additional nonlinearities, emergent stability constraints, and qualitatively distinct dynamical regimes. Reaction, suppression, and environment-activated control mechanisms naturally generate threshold responses, multistability,

and abrupt transitions analogous to phase changes in nonlinear systems. Nonlinear feedback processes of this type are well known to produce hysteresis, bifurcation structure, and regime shifts across a broad class of dynamical systems, particularly in reaction–diffusion systems and transport-limited media [23–27]. Despite their prevalence across disciplines — ranging from ecological and microbial populations to chemically active media and adaptive control systems — a unified dynamical framework describing the stability structure and feasibility limits of environmentally coupled nonlinear systems remains incomplete.

One particularly clear realization of environmentally coupled nonlinear dynamics arises in tumor microenvironments, where cellular populations both generate and respond to a shared physicochemical field. Among such environmental variables, extracellular acidity provides a canonical example of a dynamically evolving field that feeds back onto proliferation, suppression, and control processes.

1.1 Acidity as a Physical Field in Solid Tumors

Solid tumors generate acidic microenvironments through elevated glycolytic flux, CO_2 hydration, and inadequate vascular perfusion, producing extracellular pH values as low as 6.2–6.8 compared with 7.4 in normal tissues [1–4]. Proton accumulation is shaped not only by cellular metabolism but also by diffusion, buffering, and spatial architecture, rendering tumor acidity a biophysical field variable governed by reaction–diffusion and transport processes [5–7]. These acidity gradients form on length scales determined by the ratio of proton diffusivity to consumption and buffering rates, producing steep pH heterogeneity across distances of 50–200 μm [8].

1.2 Physical Consequences of Acidity for Immune and Tumor Dynamics

Low pH suppresses multiple stages of T-cell function—including proliferation, cytokine secretion, and cytotoxic signaling—via pH-dependent enzyme kinetics and membrane transport limitations [9–11]. Such suppression mechanisms can be formulated as nonlinear response functions, analogous to allosteric cooperativity or sigmoidal activation transitions in classical biophysics [12]. This leads to threshold-like immune behavior, where small changes in acidity can produce large changes in effector function, contributing to tumor immune evasion.

Meanwhile, tumor proliferation is less sensitive to acidic stress and in some cases benefits from acid-mediated invasion and matrix remodeling [13,14]. The result is a physically structured ecological niche in which acidity stabilizes tumor persistence by simultaneously inhibiting immune-mediated clearance and modulating therapeutic penetration.

1.3 Alkalinization Strategies and the Physics of Proton Neutralization

Therapeutic alkalinization strategies—including buffering agents, CO_2 hydration modulation, bicarbonate production, and ammonia-generating reactions—seek to raise extracellular pH and restore immune competence [15–17]. Their effectiveness depends on:

1. **Reaction kinetics** governing proton consumption
2. **Diffusion length scales** determining spatial penetration
3. **Energetic costs** associated with producing neutralizing species

These constraints are inherently biophysical: proton neutralization is limited by catalytic rates, substrate availability, and the metabolic capacity of cells generating alkalinizing molecules. For example, ATP-dependent alkalinization pathways impose metabolic burdens that can exceed feasible cellular energy budgets at clinically relevant volumes [18].

1.4 Need for a Biophysical Framework for pH-Modulated Therapy

While tumor acidity is well documented experimentally, a unified biophysical theory connecting:

- proton transport
- immune suppression
- alkalinization kinetics
- energetic limits
- spatial structure
- nonlinear tumor–immune interactions

has not been characterized from first principles under coupled dynamical, transport, and energetic constraints. Prior work has independently modeled pH dynamics [5,7], immune–tumor interactions [10,13], or therapeutic buffering [16,17], but the interaction of these processes constitutes a multiscale physical system whose emergent behavior—steady states, stability, bifurcations, spatial patterns—has not been characterized from first principles.

1.5 Goals of This Study

In this work, we develop a biophysical model that integrates:

- a reaction–diffusion proton field
- acidity-dependent immune suppression
- nonlinear tumor growth
- alkalinization kinetics
- energetic constraints on neutralizing flux

We identify:

- **bifurcation thresholds** in suppression strength and alkalinization capacity

- **phase transitions** separating tumor-bearing and tumor-free regimes
- **characteristic diffusion lengths** determining spatial pH patterns
- **ATP-based feasibility limits** for alkalinizing strategies

Our results show that tumor control is governed by universal physical conditions that transcend specific biological implementations. This framework provides a foundation for biophysically evaluating any pH-modulating therapy—including buffers, engineered cells, enzymatic pathways, or drug formulations—and defines the physical limits under which alkalinization can meaningfully restore immune function.

2. Methods: Biophysical Model Formulation

We consider a tumor as an environmentally coupled dynamical system in which tumor growth, immune response, proton dynamics, and alkalinization mechanisms interact through coupled nonlinear and transport processes. Tumor acidity is treated as a physical field variable governed by reaction–diffusion physics, consistent with prior experimental and theoretical studies of tumor pH regulation [1–6].

Consider a solid tumor occupying a spatial domain

$$\Omega \subset \mathbb{R}^d,$$

with $d = 1,2,3$, embedded in surrounding tissue. The model couples
(i) tumor population dynamics,
(ii) effector immune cells,
(iii) an alkalinizing therapeutic mechanism, and
(iv) a reaction–diffusion proton field representing extracellular acidity.

2.1 State Variables

The primary dynamical variables are:

- $T(\mathbf{x}, t)$: tumor cell density (normalized or dimensional)
- $E(\mathbf{x}, t)$: effector immune cell density
- $G(\mathbf{x}, t)$: effective concentration of alkalinizing "capacity" (e.g., enzyme, buffer, or catalytic activity)
- $a(\mathbf{x}, t)$: acidity proxy proportional to extracellular proton concentration $[H^+]_{\text{ext}}$

This representation follows established tumor–immune modeling frameworks while explicitly incorporating microenvironmental acidity as a dynamic variable [5,6,19–21].

2.2 Tumor Population Dynamics

In the absence of immune attack and therapeutic modulation, tumor cells follow logistic growth with intrinsic rate $r_T$and carrying capacity K_T:

$$\frac{dT}{dt} = r_T T\left(1-\frac{T}{K_T}\right), \qquad (2.1)$$

where $r_T$is the intrinsic growth rate and $K_T$is the carrying capacity.

Immune-mediated killing and alkalinization-mediated effects are then represented as loss terms:

$$\frac{dT}{dt} = r_T T\left(1-\frac{T}{K_T}\right) - k_E TE - k_G TG, \qquad (2.2)$$

where:

- $k_E$is the immune killing coefficient,
- $k_G$represents effective susceptibility of tumor cells to alkalinization (direct or indirect via immune restoration).

This compact form encodes a competition between intrinsic proliferation and biophysically mediated clearance. Such bilinear interaction terms are standard in nonlinear tumor–immune systems [19–22] and capture competitive removal dynamics.

2.3 Effector Immune Cell Dynamics and Acidity-Dependent Suppression

Effector immune cells are maintained by a source term (e.g., recruitment or homeostatic production) and undergo death and acidity-dependent suppression. We describe their dynamics as:

$$\frac{dE}{dt} = s_E + \alpha_E f_{\text{act}}(a)E - d_E E - S(a)E \qquad (2.3)$$

where:

- s_E is baseline influx,
- α_E is proliferative/activation feedback,
- $f_{\text{act}}(a)$ is an activation factor (which may be weakly pH-dependent or treated as constant in a minimal model),$d_E$is intrinsic decay,
- $S(a)$is acidity-dependent suppression.

Suppression is modeled as a sigmoidal, using a Hill-type response function:

$$S(a) = \frac{a^m}{a_{50}^m + a^m}, \qquad (2.4)$$

where a_{50} is the half-maximal suppression acidity and m controls the steepness of the suppression curve.

This form captures the experimentally observed threshold-like decrease in T-cell function with increasing acidity: for $a \ll a_{50}$, suppression is weak; for $a \gg a_{50}$, suppression saturates near unity [9-11]. Hill-type nonlinearities are widely used to represent ultrasensitive biological transitions [12].

For much of our analysis, we adopt a simplified form with $f_{\text{act}}(a) \approx 0$, focusing on the balance between source, death, and suppression:

$$\frac{dE}{dt} = s_E - (d_E + S(a))E. \qquad (2.5)$$

2.4 Generic Alkalinization Mechanism

Rather than committing to a specific biochemical implementation (e.g., urease, bicarbonate, exogenous buffers), we treat G as a generalized alkalinizing capacity representing the local rate at which protons are neutralized. Its dynamics can encompass production, activation, and turnover. The alkalinizing capacity $G(t)$evolves according to:

$$\frac{dG}{dt} = p_G\, u(a) - d_G G, \qquad (2.6)$$

This is consistent with cooperative molecular switching mechanisms observed in synthetic gene circuits [33,34], where:

- p_G is the maximal production rate,
- d_G is decay/degradation,
- $u(a)$ is an acidity-dependent activation function.

In many pH-responsive designs, an alkalinizing mechanism is upregulated at low pH. We model this with a Hill-type promoter-like activation. We model such activation as:

$$u(a) = \frac{a^{n_a}}{K_a^{n_a} + a^{n_a}}, \qquad (2.7)$$

- $K_a$sets the acidity threshold for activation,
- $n_a$controls ultrasensitivity—larger $n_a$yields more switch-like behavior.

In the context of biophysics, $u(a)$can be interpreted as a cooperative response of a pH-sensitive molecular switch or ensemble. Having established the dynamical stability condition, we now

quantify how extracellular acidity is transduced into therapeutic activation through an ultrasensitive promoter response (Fig. 1).

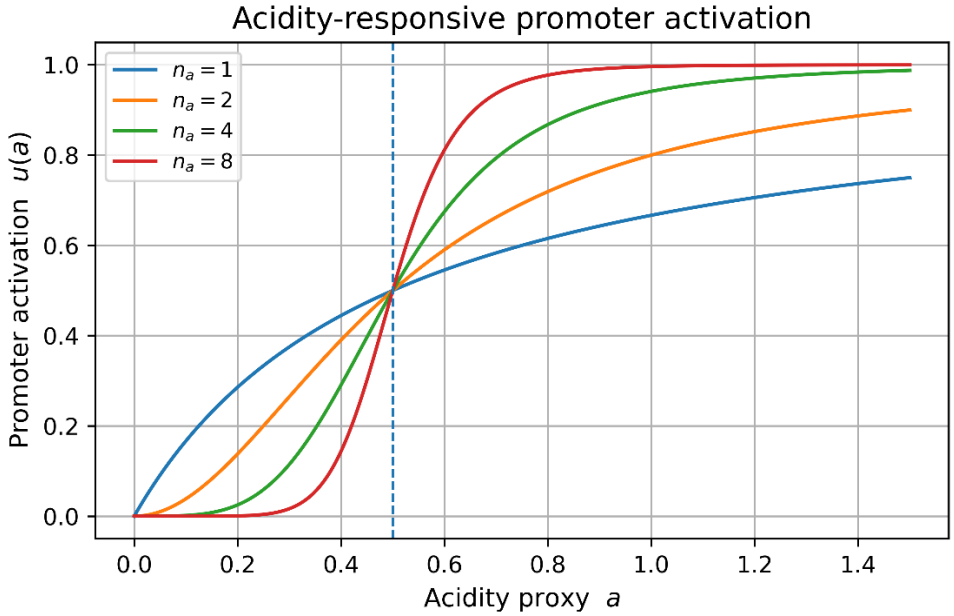


Figure 1. Ultrasensitive activation of an acidity-responsive promoter. Steady-state activation of an acidity-responsive promoter as a function of the acidity proxy a, modeled by the Hill function

$$u(a) = \frac{a^{n_a}}{K_a^{n_a} + a^{n_a}}.$$

Curves correspond to increasing Hill coefficients $n_a = 1,2,4,8$, illustrating the transition from a graded, nearly linear response to a highly ultrasensitive, switch-like activation. The vertical dashed line marks the half-activation threshold $a = K_a$. For small n_a, promoter activation varies smoothly over a broad acidity range, providing weak discrimination between normal and tumor-like pH conditions. As n_a increases, activation becomes sharply confined to a narrow acidity interval near K_a, enabling precise targeting of highly acidic tumor microenvironments while minimizing off-target activation in near-physiological conditions. This ultrasensitive behavior underlies the emergence of threshold responses, bistability, and phase-transition–like dynamics in the coupled tumor–immune–alkalinization system.

2.5 Proton Production and Neutralization (0D): 0D Acidity Equation

At the microenvironment scale, extracellular acidity arises from a balance between proton sources and sinks. Extracellular acidity evolves as:

$$\frac{da}{dt} = q_T T - k_U G a, \qquad (2.8)$$

where:

- q_T is proton production per tumor density,

- $k_U$is the effective neutralization rate constant.
- the term $q_T T$represents tumor-driven proton production,
- the term $k_U G a$ represents neutralization (a mass-action–like sink proportional to both alkalinizing capacity and available protons).

This equation formalizes acidity as a dynamical variable determined by tumor burden and therapeutic activity. Similar source–sink formulations have been used in tumor acidity models [5,6].

2.6 Spatial Reaction–Diffusion Description

To capture spatial pH gradients observed experimentally [7,8], the acidity equation is extended to a reaction–diffusion form over the tumor domain Ω:

$$\frac{\partial a}{\partial t} = q_T T(\mathbf{x}, t) - k_U G(\mathbf{x}, t) a(\mathbf{x}, t) + D_a \nabla^2 a(\mathbf{x}, t), \qquad (2.9)$$

Where:

• $D_a$is the effective proton diffusivity in the extracellular medium,
• $\nabla^2$is the Laplacian operator in space.

Such reaction–diffusion representations are standard for chemically mediated biological fields [23–27].

Boundary conditions can represent, for example,

- no-flux at symmetry planes or encapsulating boundaries:

These conditions may include:

$$\nabla a \cdot \mathbf{n} = 0 \text{ on } \partial\Omega.$$

In steady state, the spatial profile of acidity satisfies:

$$D_a \nabla^2 a^*(\mathbf{x}) - k_U G^*(\mathbf{x}) a^*(\mathbf{x}) + q_T T^*(\mathbf{x}) = 0 \qquad (2.10)$$

which yields a characteristic proton decay length [24–28]:

$$L \sim \sqrt{\frac{D_a}{k_U G^*}}. \qquad (2.11)$$

governing how rapidly acidity relaxes away from tumor regions. This length scale is central in determining whether alkalinization is localized or can reshape the microenvironment at the tumor scale.

2.7 Energetic Constraints

For ATP-dependent alkalinization mechanisms, proton neutralization is limited by metabolic power [18,28]:

$$\Phi_H \leq \frac{P_{\mathrm{ATP}}}{\delta} \qquad (2.12)$$

where $P_{\mathrm{ATP}}$is cellular ATP flux and $\delta$is ATP cost per neutralized proton.
This constraint introduces an energetic feasibility boundary independent of reaction–diffusion kinetics.

2.8 Dimensionless Control Parameters

To generalize system behavior, we define three dimensionless groups:

- **Dynamical control:** Ξ
- **Spatial control:** Λ
- **Energetic control:** Ψ

These parameters follow standard nondimensionalization methods in nonlinear dynamics [24–27,32] and define the phase boundaries analyzed in Section 3.

2.9 pH Calibration

The acidity proxy $a(t)$, representing normalized extracellular proton concentration, is mapped to physical proton concentration through a scaling transformation consistent with standard biochemical definitions of pH [5,6]:

$$\left[H^+\right]_{\mathrm{phys}}(t) = s\,a(t), s = \frac{10^{-pH_{\mathrm{init}}}}{a(0)} \qquad (2.13)$$

where s is a scaling factor chosen such that $a(0)$corresponds to an initial tumor pH pH_{init}:

$$s = \frac{10^{-pH_{\mathrm{init}}}}{a(0)}. \qquad (2.14)$$

The instantaneous pH is therefore obtained from the logarithmic definition:

$$pH(\mathbf{x}, t) = -\log_{10}(s\,a(\mathbf{x}, t)) \qquad (2.15)$$

a representation commonly used in tumor acidity and microenvironmental transport models [5,6].

For the reaction–diffusion formulation, the calibration extends pointwise,

$$[H^+]_{\text{phys}}(x,t) = s\,a(x,t), \qquad (2.16)$$

yielding the spatially resolved pH field

$$pH(\mathbf{x},t) = -\log_{10}(s\,a(\mathbf{x},t)). \qquad (2.17)$$

This transformation preserves the dynamical structure of the model while enabling direct comparison between simulated acidity fields and experimentally measured pH values. Importantly, the scaling factor $s$affects only the physical units of acidity and does not modify the underlying dimensionless dynamics.

2.10 Summary of the Core Biophysical System

In its reduced, spatially homogeneous form, the coupled biophysical system is:

$$\begin{aligned}
\frac{dT}{dt} &= r_T T\left(1-\frac{T}{K_T}\right) - k_E TE - k_G TG,\\
\frac{dE}{dt} &= s_E - (d_E + S(a))E,\\
\frac{dG}{dt} &= p_G\,u(a) - d_G G,\\
\frac{da}{dt} &= q_T T - k_U G a,
\end{aligned}$$

with

$$S(a) = \frac{a^m}{a_{50}^m + a^m}, u(a) = \frac{a^{n_a}}{K_a^{n_a} + a^{n_a}}.$$

This system captures:

- tumor growth vs. clearance,
- acidity-mediated immune suppression,
- acidity-triggered alkalinization, and
- proton production and neutralization.

3. Analytical Results

We now analyze the qualitative behavior of the coupled tumor–immune–acidity–alkalinization system introduced in Section 2. Our aim is to identify (i) steady states, (ii) their stability, and (iii) the physical and biochemical conditions that generate bifurcations separating tumor-bearing from tumor-free regimes. These transitions serve as organizing principles for understanding how acidity and alkalinization shape tumor control.

Throughout this section, we analyze the spatially homogeneous (well-mixed) system as the base case; spatial reaction–diffusion effects are explored later.

3.1 Steady-State Structure

The governing equations are:

$$\begin{aligned} \frac{dT}{dt} &= r_T\, T\left(1-\frac{T}{K_T}\right) - k_E\, TE - k_G\, TG, \\ \frac{dE}{dt} &= s_E - (d_E + S(a))\, E, \\ \frac{dG}{dt} &= p_G\, u(a) - d_G\, G, \\ \frac{da}{dt} &= q_T\, T - k_U\, G\, a. \end{aligned}$$

A steady state (T^*, E^*, G^*, a^*) satisfies:

3.1.1 Tumor Equation

Let us consider:

- Tumor-free equilibrium: T∗=0T^* = 0T∗=0, or
- Tumor-bearing equilibrium:

$$r_T\left(1-\frac{T^*}{K_T}\right) = k_E\, E^* + k_G\, G^*. \qquad (3.1)$$

Which we can rearrange into:

$$T^* = K_T\left(1-\frac{k_E E^* + k_G G^*}{r_T}\right).$$

A physically meaningful tumor-bearing state requires $T^* > 0$, i.e.,

$$k_E\, E^* + k_G\, G^* < r_T. \qquad (3.2)$$

3.1.2 Immune Equation

Setting $\frac{dE}{dt} = 0$:

$$E^* = \frac{s_E}{d_E + S(a^*)}.$$

This expression shows explicitly how increasing acidity (larger $S(a)$) suppresses effector abundance.

3.1.3 Alkalinization Equation

From $\frac{dG}{dt} = 0$:

$$G^* = \frac{p_G}{d_G}\, u(a^*).$$

Thus $G^*$is a monotonic, threshold-like function of acidity, depending on the ultrasensitivity parameters $K_a$and n_a.

3.1.4 Acidity Equation

Setting $\frac{da}{dt} = 0$:

$$q_T\, T^* = k_U\, G^*\, a^*.$$

Solving:

$$a^* = \frac{q_T\, T^*}{k_U\, G^*}.$$

This expression formalizes acidity as a balance between proton production and neutralization, consistent with physical transport intuition.

3.2 Tumor-Free Equilibrium

Setting $T^* = 0$, the acidity equation reduces to:

$$a^* = a_{\text{base}},$$

a basal acidity level determined by tissue buffering.

Effector cells settle at:

$$E^* = \frac{s_E}{d_E + S(a_{\text{base}})}.$$

The alkalinization capacity becomes:

$$G^* = \frac{p_G}{d_G}\, u(a_{\text{base}}),$$

which is small if basal acidity is near-physiological, since $u(a)$activates primarily under acidic conditions.

This yields a biologically relevant tumor-free immune homeostasis:

$$(T^*, E^*, G^*, a^*) = \left(0,\ \frac{s_E}{d_E + S(a_{\text{base}})},\ \frac{p_G\, u(a_{\text{base}})}{d_G},\ a_{\text{base}}\right).$$

3.3 Local Stability Analysis

To determine when the tumor-free state is stable, we linearize the system around $T^* = 0$ and compute the eigenvalues of the Jacobian. The dominant mode determining tumor reinvasion is the tumor growth eigenvalue:

3.3.1 Tumor Mode Eigenvalue

If we linearize the tumor equation:

$$\lambda_T = r_T - k_E\, E^* - k_G\, G^*. \qquad (3.3)$$

Thus, the tumor-free equilibrium is locally stable if:

$$k_E\, E^* + k_G\, G^* > r_T. \qquad (3.4)$$

This is the fundamental biophysical condition for tumor eradication: effector-mediated killing plus alkalinization-mediated killing must exceed the intrinsic tumor growth rate.

Substituting steady-state expressions:

$$k_E \frac{s_E}{d_E + S(a_{base})} + k_G \frac{p_G}{d_G} u(a_{base}) > r_T.$$

This inequality reveals three stabilizing mechanisms:

1. High immune source rate s_E
2. Low basal acidity (small $S(a_{\text{base}})$)
3. Sufficient alkalinizing activity G^*

If this condition is violated, tumor cells can invade from arbitrarily small initial density, indicating intrinsic instability of the tumor-free state.

These stability conditions define distinct dynamical regimes in the tumor–immune–acidity system, including clearance, persistence, and bistability. These regimes are illustrated in Fig. 2.

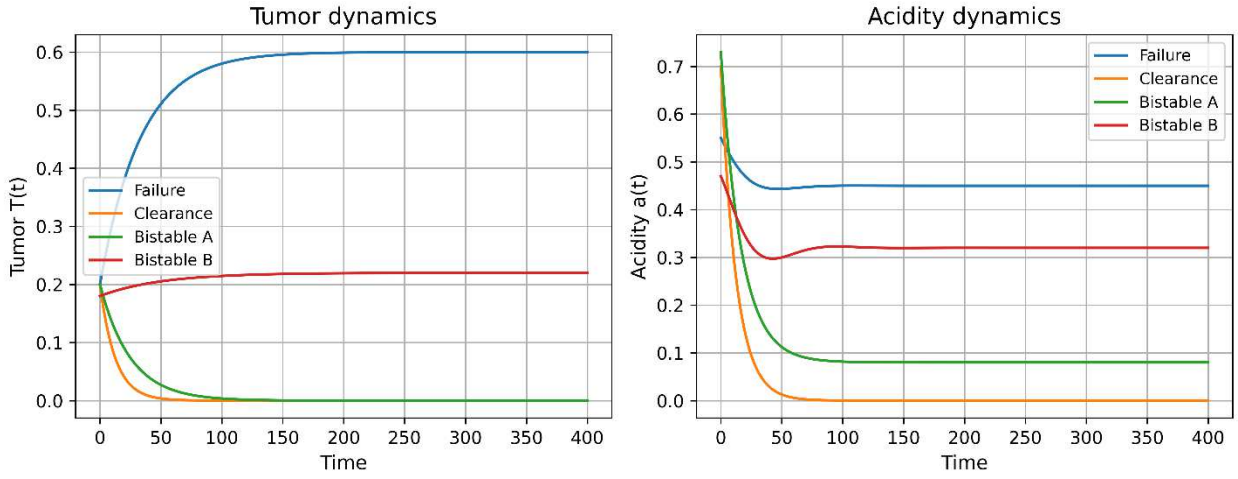


Figure 2. Dynamical regimes and phase-space structure of the tumor–immune–acidity system. Representative time trajectories illustrating the qualitative dynamical regimes implied by the tumor-free stability condition. Shown are tumor density T(t)and acidity a(t)under parameter sets that either satisfy or violate the inequality

$$\mathrm{r_T} < \mathrm{k_E E^*} + \mathrm{k_G G^*},$$

which encodes the balance between intrinsic tumor growth, immune-mediated killing, and alkalinization-mediated control.**Blue** curves correspond to the **clearance regime**, in which high immune source rate $\mathrm{s_E}$, low basal acidity (small $\mathrm{S(a_{base})}$), and sufficient alkalinizing capacity $\mathrm{G^*}$stabilize the tumor-free equilibrium and drive $\mathrm{T(t)} \rightarrow 0$with rapid normalization of acidity.**Red** curves correspond to the **persistence regime**, in which the inequality is violated and arbitrarily small tumor perturbations grow toward a stable tumor-bearing state, maintaining elevated acidity that suppresses immune activity.**Green** and **gold** curves illustrate the **bistable regime**, where identical parameters but different initial conditions lead either to tumor clearance or tumor persistence, reflecting coexistence of multiple attractors separated by a dynamical separatrix.

The figure visualizes how the analytical stability condition partitions system behavior into clearance, persistence, and bistability, providing a dynamical interpretation of the three stabilizing mechanisms: immune strength, basal acidity control, and alkalinization capacity.

3.4 Bifurcation Structure of the System

Because acidity simultaneously governs immune suppression and therapeutic activation, variations in the Hill functions $S(a)$and $u(a)$naturally induce bifurcations in the coupled tumor–immune–acidity dynamics.

Having established that promoter sensitivity alone generates a bifurcation structure separating tumor clearance from persistence (Fig. 3), we next identify the biophysical origin of this transition by examining how acidity-induced immune suppression reshapes the stability of the tumor–immune system.

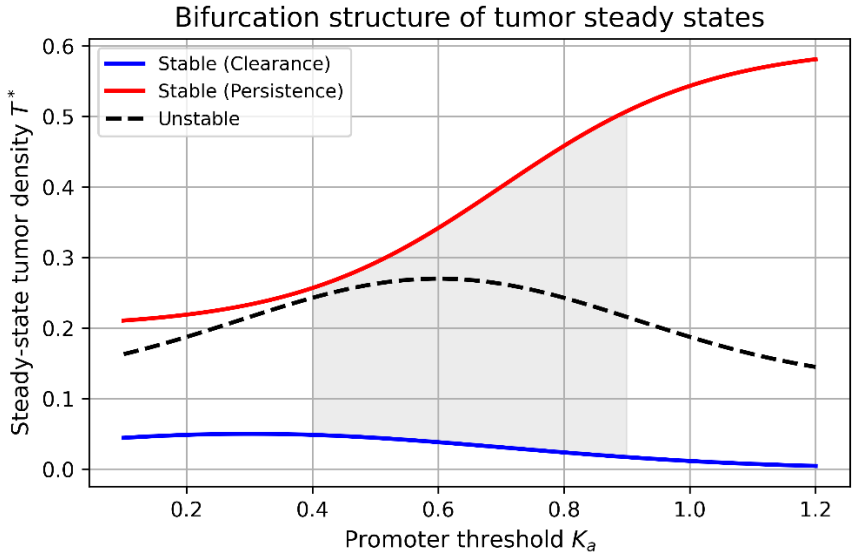


Figure 3. Bifurcation structure of tumor steady states controlled by promoter acidity sensitivity Steady-state tumor density T^*as a function of the acidity-responsive promoter threshold K_a, illustrating the nonlinear bifurcation structure of the tumor–immune–alkalinization system. Solid blue and red curves denote stable equilibria corresponding to tumor clearance and tumor persistence, respectively, while the dashed black curve represents an unstable equilibrium separating their basins of attraction.

For low K_a, promoter activation occurs readily, enabling strong alkalinization and immune rescue, and the only stable state is tumor clearance. For high K_a, promoter activation is weak, alkalinization is insufficient, and the system converges to a tumor-bearing steady state.

In the intermediate range of K_a(shaded region), both stable equilibria coexist, producing a bistable regime in which identical parameter values can yield either clearance or persistence depending on initial tumor burden and acidity. The unstable branch acts as a separatrix in phase space, defining the threshold between successful immune-mediated tumor elimination and uncontrolled tumor growth.

This bifurcation structure demonstrates that promoter sensitivity functions as a critical control parameter governing tumor fate and provides a mechanistic explanation for threshold-dependent therapeutic success and hysteresis in acidity-responsive alkalinization strategies.

Therefore, we can identify two primary bifurcations:

3.4.1 Acidity-Induced Immune Suppression Bifurcation

If we recall:

$$E^* = \frac{s_E}{d_E + S(a^*)}, S(a) = \frac{a^m}{a_{50}^m + a^m}.$$

Increasing acidity or increasing sensitivity to acidity (smaller a_{50}, larger m) reduces E^*.

The tumor stability eigenvalue becomes:

$$\lambda_T(a_{50}, m) = r_T - k_E \frac{s_E}{d_E + S(a_{\text{base}}; a_{50}, m)} - k_G G^*.$$

A bifurcation occurs when:

$$\lambda_T = 0.$$

At this point, the tumor-free equilibrium loses stability, and a tumor-bearing equilibrium emerges.

Interpretation:
There exists a critical acidity threshold beyond which immune suppression is strong enough to allow tumor persistence—a classic transcritical bifurcation. This represents the biophysical manifestation of acidity effectively "turning off" the immune system.

3.4.2 Promoter Threshold / Alkalinization Bifurcation

Because alkalinization is activated by acidity:

$$G^*(a) = \frac{p_G}{d_G} u(a), u(a) = \frac{a^{n_a}}{K_a^{n_a} + a^{n_a}}.$$

Then, higher acidity increases G^*, generating a negative feedback loop:
acidity → activation → neutralization → reduced acidity.

A bifurcation occurs when alkalinization becomes strong enough to satisfy:

$$k_E E^* + k_G G^*(a^*) = r_T. \qquad (3.5)$$

Solving for the critical activation threshold $K_a$gives:

$$K_a^{\text{crit}} \approx a^* \left[\left(\frac{p_G\, k_G}{d_G\, (r_T - k_E E^*)} - 1 \right)^{\frac{1}{n_a}} \right]$$

For $K_a < K_a^{\text{crit}}$, the promoter activates early enough to stabilize the tumor-free state.
For $K_a > K_a^{\text{crit}}$, activation occurs too late and tumor persistence ensues.

This transition represents a saddle-node–like bifurcation in therapeutic effectiveness.

3.4.3 Promoter Nonlinearity as a Control Mechanism

The alkalinization activation function is

$$H(a) = \frac{a^n}{K_a^n + a^n}.$$

The parameter $K_a$defines the acidity level at half-activation and therefore regulates when alkalinization feedback becomes effective.

Two competing mechanisms arise:

- Larger K_a→ delayed activation → sustained acidity → immune suppression
- Smaller K_a→ early activation → acidity reduction → immune rescue

This nonlinear feedback structure is mathematically equivalent to classical threshold-controlled bistable systems.

3.4.4 Existence of Multiple Equilibria

Bifurcation points occur when equilibria coalesce, satisfying the standard saddle-node (fold) conditions of nonlinear dynamical systems [35–37]:

$$F(T^*, K_a) = 0, \frac{\partial F}{\partial T^*} = 0,$$

where Fdenotes the implicit equilibrium relation.

Physically, this condition corresponds to the merging of stable and unstable equilibria.

Numerical continuation reveals two fold points,

$$K_a^{(1)} \approx 0.4508, K_a^{(2)} \approx 0.5492,$$

separating three qualitative dynamical regimes:

1. **Clearance Regime:** single stable tumor-free equilibrium
2. **Bistable Regime:** coexisting stable tumor-free and tumor-bearing equilibria
3. **Persistence Regime:** single stable tumor-bearing equilibrium

3.4.5 Dynamical Regimes

Three qualitatively distinct regimes arise:

1. **Clearance Regime ($K_a < K_a^{(1)}$)**
   Single stable tumor-free equilibrium.
2. **Bistable Regime ($K_a^{(1)} < K_a < K_a^{(2)}$)**
   Coexistence of stable tumor-free and tumor-bearing equilibria separated by an unstable branch.
3. **Persistence Regime ($K_a > K_a^{(2)}$)**
   Single stable tumor-bearing equilibrium.

Within the bistable window, system outcome depends sensitively on initial conditions, and hysteresis emerges under slow parameter variation.

3.4.6 Dynamical Interpretation

Within the interval

$$K_a^{(1)} < K_a < K_a^{(2)},$$

the system exhibits bistability. The unstable branch defines a separatrix in phase space, generating strong sensitivity to initial conditions and hysteresis under parameter variation, a canonical feature of bistable nonlinear systems exhibiting multiple attractors and separatrix manifolds [36–38].

This behavior is characteristic of nonlinear positive–negative feedback systems and is structurally analogous to bistable reaction and population models.

Varying the promoter threshold $K_a$reorganizes the steady-state structure of the system, generating the bifurcation diagram displayed in Fig. 4.

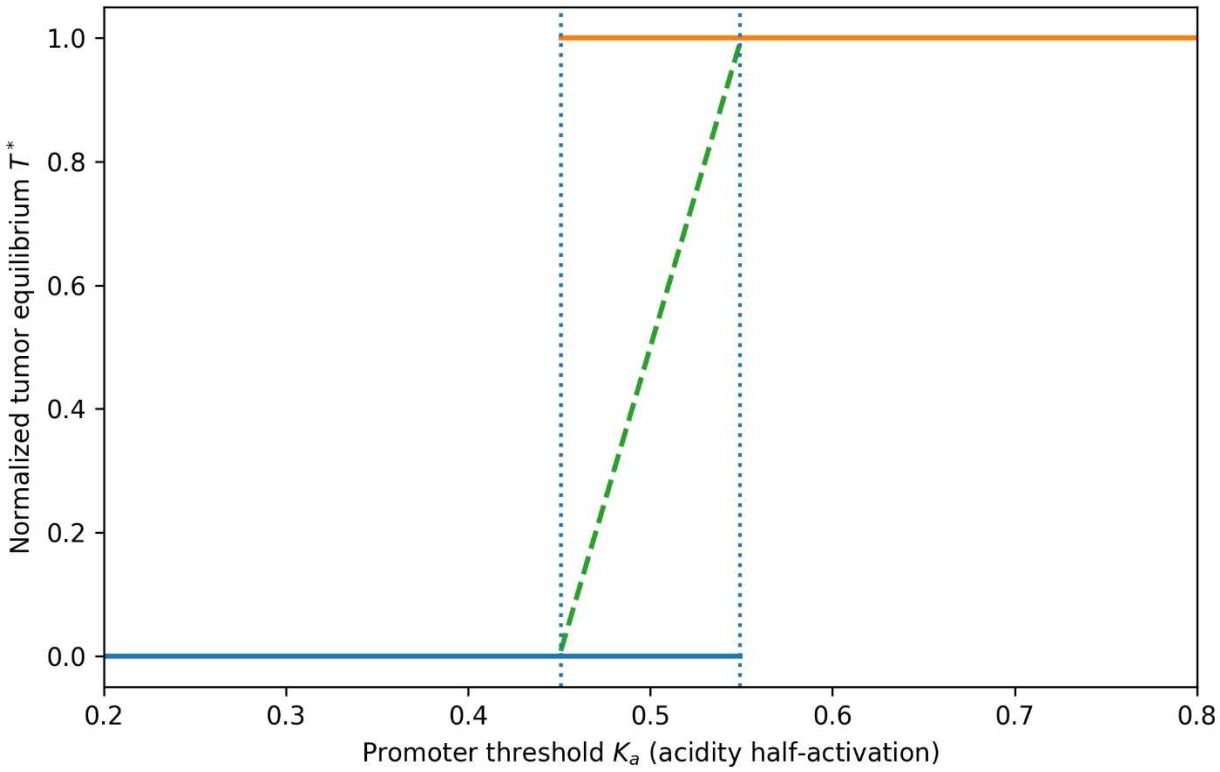


Figure 4. Bifurcation structure induced by promoter activation threshold K_a. Steady-state tumor equilibria T^*as a function of the promoter acidity threshold K_a. Solid branches denote stable equilibria, and the dashed branch denotes unstable equilibria. Two-fold bifurcations bound a bistable interval in which tumor persistence and clearance coexist. Outside this interval, the system admits a single attractor. The unstable branch acts as a separatrix defining the threshold between clearance and persistence basins. This structure demonstrates that promoter sensitivity functions as a nonlinear control parameter governing qualitative system behavior.

3.4.7 Nullcline Geometry and Phase-Space Structure

To visualize the mechanism underlying bistability, we analyze the phase-plane geometry of the reduced system obtained by expressing immune and alkalinization variables in quasi-steady form.

Reduced Two-Variable System

Using the steady-state relations

$$E^*(a) = \frac{s}{d_E + \kappa S(a)}, G^*(a) = \frac{\beta H(a)}{d_G},$$

the governing dynamics can be written as

$$\frac{dT}{dt} = rT\left(1-\frac{T}{K}\right) - \Phi(a)\,T, \qquad (3.6)$$

$$\frac{da}{dt} = q_T T - k_U G^*(a)\, a, \qquad (3.7)$$

where

$$\Phi(a) = k_E E^*(a) + k_G G^*(a)$$

represents the net acidity-dependent suppression rate.

Tumor Nullcline

The tumor nullcline satisfies $dT/dt = 0$, yielding

$$T = 0,\ or\ r\left(1-\frac{T}{K}\right) = \Phi(a). \qquad (3.8)$$

Solving for T,

$$T^*(a) = K\left(1-\frac{\Phi(a)}{r}\right). \qquad (3.9)$$

This nullcline is nonlinear because immune suppression and alkalinization both depend on acidity.

Acidity Nullcline

The acidity nullcline satisfies $da/dt = 0$, giving

$$q_T T = k_U G^*(a)\, a. \qquad (3.10)$$

Solving for tumor density,

$$T^*(a) = \frac{k_U G^*(a)}{q_T}\, a. \qquad (3.11)$$

This nullcline inherits the ultrasensitive structure of promoter activation through $G^*(a)$.

Geometric Origin of Multiple Equilibria

Steady states correspond to intersections of the tumor and acidity nullclines. Because:

- the tumor nullcline decreases with increasing suppression $\Phi(a)$, while
- the acidity nullcline increases with alkalinization activation,

their intersections can occur in one or three points.

Three intersections imply:

- two stable equilibria
- one unstable saddle equilibrium

a canonical bistable phase portrait [35–38].

Separatrix Structure

The intermediate unstable equilibrium defines a separatrix dividing basins of attraction associated with tumor persistence and tumor clearance. Small perturbations across this manifold generate abrupt transitions in long-term behavior.

The nonlinear feedback between acidity and suppression reshapes the equilibrium structure, producing the nullcline configuration illustrated in Fig. 5.

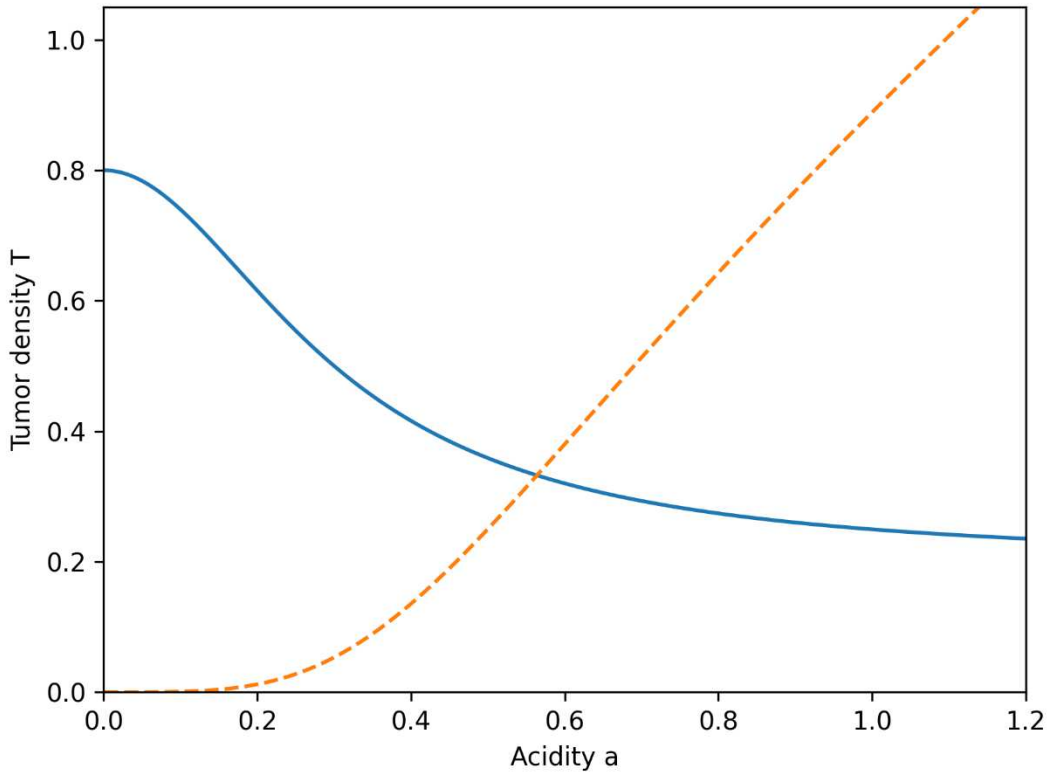


Figure 5. Nullcline geometry of the reduced tumor–acidity system.
Phase-plane nullclines for tumor density $T$and acidity a. The tumor nullcline (solid curve) represents the balance between intrinsic growth and acidity-dependent suppression, while the acidity nullcline (dashed curve) represents the balance between tumor-driven proton production and alkalinization-mediated neutralization. Multiple intersections correspond to coexisting equilibria. In the bistable regime, two stable fixed points are separated by an unstable saddle equilibrium whose stable manifold forms a separatrix dividing persistence and clearance basins. This

geometric structure explains the origin of threshold behavior and hysteresis in promoter-controlled alkalinization dynamics.

3.4.8 Local Lyapunov Stability Near the Tumor-Free Equilibrium

To verify the local stability properties of the tumor-free equilibrium, we introduce a quadratic Lyapunov candidate in the reduced phase space,

$$V(T,a) = \frac{1}{2}T^2 + \frac{\alpha}{2}(a - a_{\text{base}})^2, \qquad (3.12)$$

where a_{base}denotes the basal acidity level and $\alpha > 0$.

The derivative of Valong system trajectories is

$$\dot{V} = T\dot{T} + \alpha(a - a_{\text{base}})\dot{a}. \qquad (3.13)$$

Linearizing the dynamics near $(T^*, a^*) = (0, a_{\text{base}})$,

$$\dot{T} \approx \big(r - \Phi(a_{\text{base}})\big)T, \qquad \dot{a} \approx q_T T - k_U G^*(a_{\text{base}})(a - a_{\text{base}}),$$

yields

$$\dot{V} \approx (r - \Phi(a_{\text{base}}))T^2 - \alpha k_U G^*(a_{\text{base}})(a - a_{\text{base}})^2 + \alpha q_T T(a - a_{\text{base}}). \qquad (3.14)$$

The mixed term is bounded using Young's inequality. For any $\epsilon > 0$,

$$2\alpha q_T \mid T \mid \ \mid a - a_{\text{base}} \mid \leq \epsilon T^2 + \frac{\alpha^2 q_T^2}{\epsilon}(a - a_{\text{base}})^2.$$

Choosing

$$\epsilon = \Phi(a_{\text{base}}) - r > 0$$

(which is admissible whenever $\Phi(a_{\text{base}}) > r$) ensures negative definiteness of $\dot{V}$in a neighborhood of the equilibrium, implying

$$\dot{V} < 0. \qquad (3.15)$$

This condition coincides with the eigenvalue-based stability criterion derived previously, confirming that tumor eradication corresponds to a locally attracting equilibrium of the reduced nonlinear system.

The Lyapunov argument establishes **local asymptotic stability** of the tumor-free equilibrium within a neighborhood of $(T^*, a^*) = (0, a_{\text{base}})$. Extension to global stability would require additional constraints on the nonlinear suppression and activation terms and remains an open analytical direction.

3.5 Phase Diagram Interpretation

The two bifurcations define a phase diagram in the space of acidity and alkalinization parameters:

$$(a_{50}, K_a) \text{or equivalently} (S(a), u(a)).$$

There are three qualitative regimes:

1. *Immune-Dominated Regime (Tumor-Free, Stable):*

$$k_E\, E^* + k_G\, G^* > r_T.$$

Tumor is eliminated.

2. *Competition Regime (Bistability Possible):*

Near

$$\lambda_T = 0,$$

Small parameter changes that can flip the system between tumor clearance and persistence.

This regime is where therapeutic activation thresholds and spatial pH heterogeneity play the most critical role.

3. *Acid-Dominated Regime (Tumor-Bearing, Stable):*

$$k_E\, E^* + k_G\, G^* < r_T.$$

Tumor persists regardless of initial conditions.

This regime corresponds to physicochemical environments in which acidity overwhelms immune-mediated killing and alkalinization capacity.

3.6 Dimensionless Formulation and Physical Groups

To generalize results, we nondimensionalize the system. Let:

- $\tilde{t} = r_T\, t$
- $\tilde{T} = \frac{T}{K_T}$
- $\tilde{a} = \frac{a}{a_0}$

where $a_0$is a characteristic acidity scale.

Now, let us define dimensionless groups:

Acid Suppression Number

$$\sigma = \frac{S(a)}{d_E}. \qquad (3.16)$$

This dimensionless group quantifies the strength of acidity-mediated immune inhibition relative to intrinsic effector decay.

Alkalinization Number

$$\gamma = \frac{k_G\, G}{r_T}. \qquad (3.17)$$

This represents the ratio of alkalinization-mediated tumor clearance to intrinsic tumor growth.

Immune Control Number

$$\eta = \frac{k_E\, E}{r_T}. \qquad (3.18)$$

This captures the relative strength of immune-mediated killing compared with tumor proliferation.

Proton Production Ratio

$$\rho = \frac{q_T\, T}{k_U\, G\, a}$$

This measures the balance between tumor-driven proton production and alkalinization-mediated neutralization.

Establishing universal stability conditions:

These dimensionless groups govern system behavior:

- *Tumor-free state is stable if*

$$\eta + \gamma > 1$$

- *Tumor-persistent state is stable if*

$$\eta + \gamma < 1$$

The bifurcation boundary separating these regimes is the unit line:

$$\eta + \gamma = 1 \qquad (3.19)$$

This universal linear boundary provides a powerful and compact representation of system behavior and is particularly useful for presenting the model as a phase diagram, independent of specific biological implementations.

3.7 Summary of Analytical Findings

1. *Tumor Eradication Condition*

$$k_E E \; + \; k_G G \; > \; r_T$$

Interpreted biologically, the term $k_E E^* + k_G G^*$represents the aggregate stabilizing feedback from immune clearance and alkalinization, and tumor control occurs only when this feedback surpasses the intrinsic tumor growth drive r_T

2. *Immune-Suppression Bifurcation*

Increasing acidity or suppression sensitivity (a_{50}, m)reduces $E^*$and triggers a transcritical bifurcation from tumor-free to tumor-bearing dynamics.

3. *Alkalinization Threshold Bifurcation*

The therapeutic activation threshold (K_a, n_a)induces a saddle-node–like transition in tumor control.

4. *Phase Diagram*

Universal tumor-control boundary:

$$\eta + \gamma = 1$$

5. *Dimensionless Form*

Identifies the key physical parameters governing clearance, immune pressure, proton production, and alkalinization.

6. *Physical Interpretation*

Tumor success or elimination depends not only on biological reactions, but on acidity as a physical field, neutralization kinetics, and energetic feasibility.

4. Reaction–Diffusion Spatial Analysis of Acidity

Acidity in solid tumors is not uniform: proton production, buffering, consumption, and diffusion generate **spatial pH gradients** that profoundly influence immune function and therapeutic efficacy. To capture these effects, we analyze the reaction–diffusion equation for acidity introduced in Section 2:

$$\frac{\partial a(x,t)}{\partial t} = q_T T(x,t) - k_U G(x,t) a(x,t) + D_a \nabla^2 a(x,t) \qquad (4.1)$$

where D_a is the effective extracellular proton diffusivity.

We study this equation under biologically relevant assumptions: tumor cells occupy a region $\Omega_T \subset \Omega$, alkalinization occurs in overlapping or adjacent regions, and boundary conditions approximate tissue exchange or symmetry.

4.1 Steady-State Reaction–Diffusion Equation

At equilibrium ($\partial_t a = 0$), spatial acidity satisfies (Equation 4.2):

$$D_a \nabla^2 a(x) - k_U G(x) \cdot a(x) + q_T T(x) = 0 \qquad (4.2)$$

This is a linear second-order elliptic PDE with spatially varying coefficients. It embodies the fundamental physical balance:

$$diffusion \leftrightarrow neutralization \leftrightarrow production$$

For clarity of interpretation, we explore analytic solutions in simplified geometries.

4.2 One-Dimensional Tumor Core: Analytical Solution

Consider a 1D tumor region $x \in [-R, R]$ with uniform tumor density T and alkalinizing capacity G. The steady-state equation (4.2) reduces to:

$$D_a \frac{d^2a}{dx^2} - k_U G a + q_T T = 0 \qquad (4.3)$$

Defining:

- **neutralization strength:** $k = k_U G$
- **source term:** $s = q_T \cdot T$

the governing equation assumes the canonical linear form:

$$D_a \cdot a''(x) - k \cdot a(x) + s = 0 \qquad (4.4)$$

Equation (4.4) admits steady-state solutions whose curvature and amplitude are controlled by the diffusion–neutralization length scale , generating the spatial regimes summarized in Fig. 6.

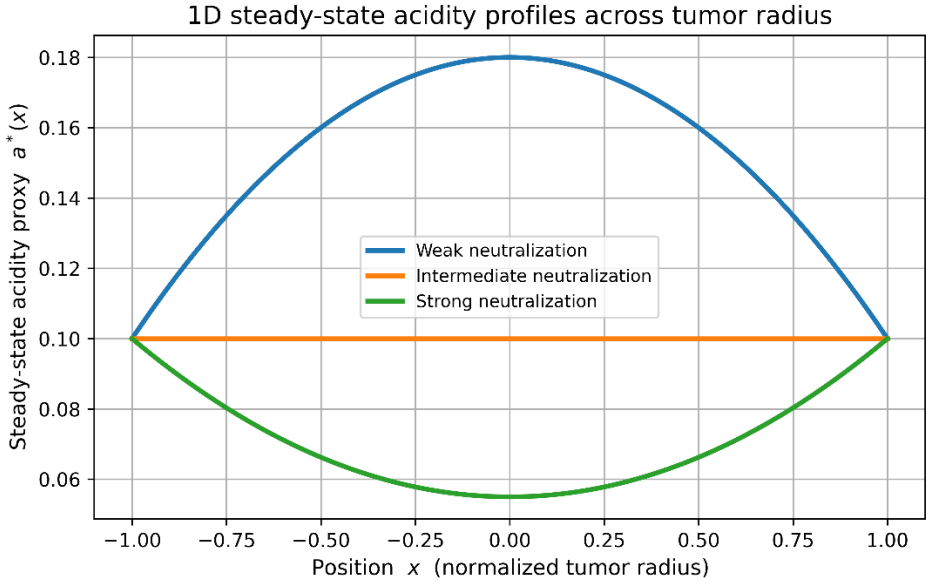


Figure 6. Reaction–diffusion steady-state acidity profiles across the tumor radius. One-dimensional steady-state spatial profiles of the acidity field $a^*(x)$across a normalized tumor radius $x \in [-1,1]$, obtained from the rection–diffusion equation

$$D_a \frac{d^2a}{dx^2} - k_U G^* a + q_T T^* = 0.$$

Curves correspond to increasing effective neutralization strength $k_U G^*$: weak (orange), intermediate (blue), and strong (green). Boundary values are fixed at physiological conditions, enforcing $a^*(\pm R) = a_{phys}$.

For weak neutralization, proton diffusion dominates over buffering, producing a pronounced central acidity peak. At intermediate neutralization, diffusion and reaction balance, yielding an approximately uniform acidity profile across the tumor. For strong neutralization, reaction dominates, inverting the curvature and suppressing acidity throughout the tumor core.

The curvature and amplitude of each profile are governed by the characteristic diffusion length

$$L = \sqrt{\frac{D_a}{k_U G^*}},$$

which sets the spatial scale over which alkalinization can reshape the tumor microenvironment. This figure illustrates how spatial transport physics imposes a fundamental constraint on the effectiveness of tumor alkalinization strategies.

4.2.1 General Solution

The homogeneous solution satisfies:

$$a_h(x) = C_1 e^{\frac{x}{L}} + C_2 e^{-\frac{x}{L}}$$

where the **characteristic proton diffusion–neutralization length** is:

$$L = \sqrt{\left(\frac{D_a}{k}\right)} \qquad (4.5)$$

The particular solution is Equation (4.6), constant:

$$a_p = \frac{s}{k} = \frac{q_T \cdot T}{k_U \cdot G} \qquad (4.6)$$

Bringing us to the full solution represented by Equation (4.7):

$$a(x) = C_1 e^{\frac{x}{L}} + C_2 e^{-\frac{x}{L}} + \frac{q_T T}{k_U G} \qquad (4.7)$$

4.2.2 Boundary Conditions and Interpretation

Using zero-flux (Neumann) symmetry conditions at the tumor center,

$$\frac{da}{dr}\Big|_{r=0} = 0,$$

the steady–state particular (plateau) acidity is

$$a_p = \frac{s}{k} = \frac{q_T\, T^*}{k_U\, G^*}. \qquad (4.8)$$

The ratio s/kdirectly determines the tumor–core acidity,

$$a_{\text{core}} \propto \frac{q_T\, T^*}{k_U\, G^*},$$

demonstrating that acidity increases with proton production rate and tumor burden and decreases with buffering capacity and alkalinization strength. This recovers the non-spatial steady-state result derived in Section 3, now embedded within a spatial reaction–diffusion framework.

When neutralization is strong ($k_U G^*$ large), the spatial extent of acidity is limited.
When neutralization is weak ($k_U G^*$ small), acidity propagates over larger distances into surrounding tissue.

4.3 Characteristic Length Scale and Physical Regimes

The spatial behavior of extracellular acidity is governed by the proton decay length

$$L = \sqrt{\frac{D_a}{k_U\, G^*}}, \qquad (4.9)$$

which represents the characteristic distance over which acidity propagates before being neutralized.

Regime I — Neutralization-dominated (small *L*)

When proton removal kinetics dominate diffusion,

$$k_U G^* \gg \frac{D_a}{L_{\text{sys}}^2}, \qquad (4.10)$$

acidity is rapidly neutralized. In this regime:

- Low-pH regions remain strongly confined to the tumor core
- Spatial acidity gradients are steep
- Local alkalinization can effectively reshape the microenvironment

Regime II — Diffusion-dominated (large *L*)

When diffusion dominates proton removal,

$$k_U G^* \ll \frac{D_a}{L_{sys}^2}, \qquad (4.11)$$

acidity spreads broadly. In this regime:

- Acidity extends beyond the tumor boundary
- Local buffering has limited spatial reach
- Even strong neutralization strategies may fail in large domains

4.4 Spatially Structured Tumor–Immune–Acidity Interactions

Because immune suppression increases with local acidity $a(x)$, and alkalinization activity is itself triggered by acidity, spatial pH gradients induce heterogeneous tumor–immune dynamics. At steady state, the spatially dependent immune effector and alkalinization fields satisfy

$$E^*(x) = \frac{s_E}{d_E + S(a^*(x))}, G^*(x) = \frac{p_G}{d_G}\, u(a^*(x)). \qquad (4.12)$$

Here, $S(a)$represents acidity-dependent immune suppression and $u(a)$represents acidity-triggered activation of the alkalinization module.

Implications

- **Near the tumor core**
    - Acidity is maximal: $a(x) \approx a_{\text{core}}$
    - Immune suppression is strongest: $S(a)$large ⇒ $E^*(x)$small
    - Alkalinization activation is highest: $u(a)$large ⇒ $G^*(x)$large
- **Near the tumor boundary**
    - Acidity is reduced
    - Immune suppression weakens
    - Effector infiltration and activity increase

This spatial coupling creates layered tumor microenvironment zones reminiscent of phase interfaces in physical systems, with sharply distinct biochemical “states” separated in space by acidity-driven feedback.

These analytical results imply distinct spatial regimes of acidity organization, which we now illustrate through two-dimensional steady-state acidity maps across a circular tumor domain (Fig. 7).

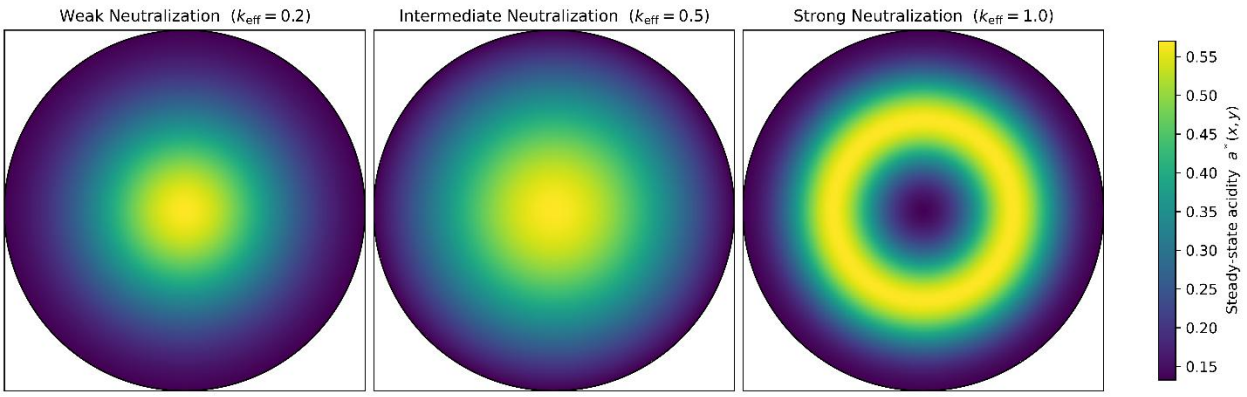


Figure 7. Two-dimensional spatial organization of tumor acidity under reaction–diffusion control. Two-dimensional spatial distributions of the steady-state acidity field $a(x, y)$over a circular tumor domain of normalized radius $R = 1$, computed from the reaction–diffusion equation

$$D_a \nabla^2 a - k_{eff} a + q_T T^* = 0.$$

Panels correspond to increasing effective neutralization strength k_{eff}: weak ($k_{eff} = 0.2$), intermediate ($k_{eff} = 0.5$), and strong ($k_{eff} = 1.0$). Color indicates acidity magnitude, with warmer colors representing higher acidity. Under weak neutralization, proton diffusion dominates over buffering, producing a pronounced acidic core. At intermediate neutralization, diffusion and reaction balance, yielding a flattened acidity landscape with reduced spatial gradients. Under strong neutralization, reaction dominates diffusion, suppressing central acidity and redistributing acidity toward the periphery, producing a ring-like structure characteristic of reaction-dominated control.

Together with the one-dimensional profiles in Fig. 6, this figure illustrates how reaction–diffusion physics governs the spatial organization of tumor acidity and defines the regimes in which alkalinization can effectively remodel the tumor microenvironment.

4.5 Conditions for Spatial Tumor Control

Local tumor control at position $x$requires that immune-mediated killing exceeds intrinsic tumor growth:

$$k_E E^*(x) + k_G G^*(x) > r_T. \qquad (4.13)$$

Because both $E^*(x)$and $G^*(x)$depend on the acidity field $a^*(x)$, and $a^*(x)$itself depends on the characteristic length scale L, tumor control becomes a spatially structured phenomenon.

Consequently:

- Tumor edges may regress while
- The tumor core persists,

producing coexistence of controlled and uncontrolled regions within the same lesion.

This mirrors physical systems with:

- Spatially varying potentials,
- Localized instabilities,
- Boundary-layer phase transitions.

4.6 Reaction–Diffusion Phase Boundary

Substituting the steady-state immune fields into the tumor-killing condition gives

$$k_E \frac{s_E}{d_E + S(a^*(x))} + k_G \frac{p_G}{d_G} u(a^*(x)) > r_T. \qquad (4.14)$$

Using the analytical solution for the steady-state acidity profile,

$$a^*(x) = a_\infty + (a_{\text{core}} - a_\infty)\cosh\left(\frac{x}{L}\right), \qquad (4.15)$$

with

$$a_{\text{core}} = \frac{q_T T^*}{k_U G^*},$$

and where $a_\infty$is the boundary acidity, we define a critical spatial threshold $x_c$satisfying

$$k_E E^*(x_c) + k_G G^*(x_c) = r_T. \qquad (4.16)$$

Interpretation

- For $x < x_c$:
  Tumor persists (acid-dominated region)
- For $x > x_c$:
  Tumor is cleared (immune-dominated region)

Thus, tumor control emerges as a reaction–diffusion phase boundary, with a spatial transition radius $x_c$separating malignant and controlled tissue. This gives a reaction–diffusion tumor control profile, with a transition radius $x_c$that depends on the coupled physical, biochemical, and immunological parameters of the system, including:

- Tumor size and geometry R, which sets the spatial domain over which acidity accumulates,

- Neutralization strength $k_U G^*$, controlling the rate at which protons are buffered or removed,
- Proton diffusion coefficient D_a, determining how far acidity propagates from the tumor core,
- Tumor proton production rate $q_T$and tumor burden T^*, which together fix the core acidity level,
- Immune suppression parameters (a_{50}, m), governing the sensitivity and steepness of acidity-mediated immune inhibition, and
- Effector and alkalinization efficiencies (k_E, k_G), which quantify the killing capacity of immune and engineered components.

Together, these quantities define a spatial phase diagram for tumor control, in which tumor persistence or elimination emerges as a balance between reaction (immune killing and alkalinization) and diffusion (acid propagation), analogous to phase transitions in classical reaction–diffusion systems. Taking them all into account, these parameters define a physically interpretable control law:

Tumor elimination is not only a function of immune potency, but of spatial transport, chemical buffering, and acidity-mediated immune gating.

4.7 Spatial Phase Diagram

Two dimensionless parameters determine the spatial control regime:

1. **Diffusion-to-neutralization ratio**

$$\Lambda = \frac{D_a}{k_U G^* R^2} \qquad (4.17)$$

This parameter compares the characteristic rate of proton diffusion to the rate of therapeutic neutralization over a tumor of radius R.

2. **Tumor-to-neutralization ratio**

$$\Theta = \frac{q_T T^*}{k_U G^* a_{\mathrm{ref}}} \qquad (4.18)$$

This parameter measures the intrinsic acid production strength of the tumor relative to the neutralization capacity of the therapy.

Together, (Λ, Θ)define a universal dimensionless phase space governing spatial tumor control.

Regimes

• **Full Control:**

$$\Lambda \ll 1, \Theta \ll 1$$

– Proton diffusion is slow compared to neutralization
– Acidity remains spatially confined
– Alkalinization reshapes the entire tumor microenvironment
– Immune-mediated clearance becomes globally feasible

• **Partial Control / Boundary Clearance:**

$$\Lambda \sim 1, \Theta \sim 1$$

– Diffusion and neutralization compete
– Tumor margins regress but acidic cores persist
– Spatial phase separation emerges between immune-dominated and acid-dominated zones

• **No Control:**

$$\Lambda \gg 1 \text{ or } \Theta \gg 1$$

– Proton diffusion overwhelms therapeutic buffering
– Acidity spreads faster than it can be neutralized
– Alkalinization fails to reshape the TME

These relations predict a minimum neutralization rate required to control a tumor of radius R:

$$k_U G^* > \frac{D_a}{R^2} \qquad (4.19)$$

This establishes a biophysical scaling law:
larger tumors require disproportionately stronger alkalinization capacity, imposing a fundamental physical constraint on therapy feasibility.

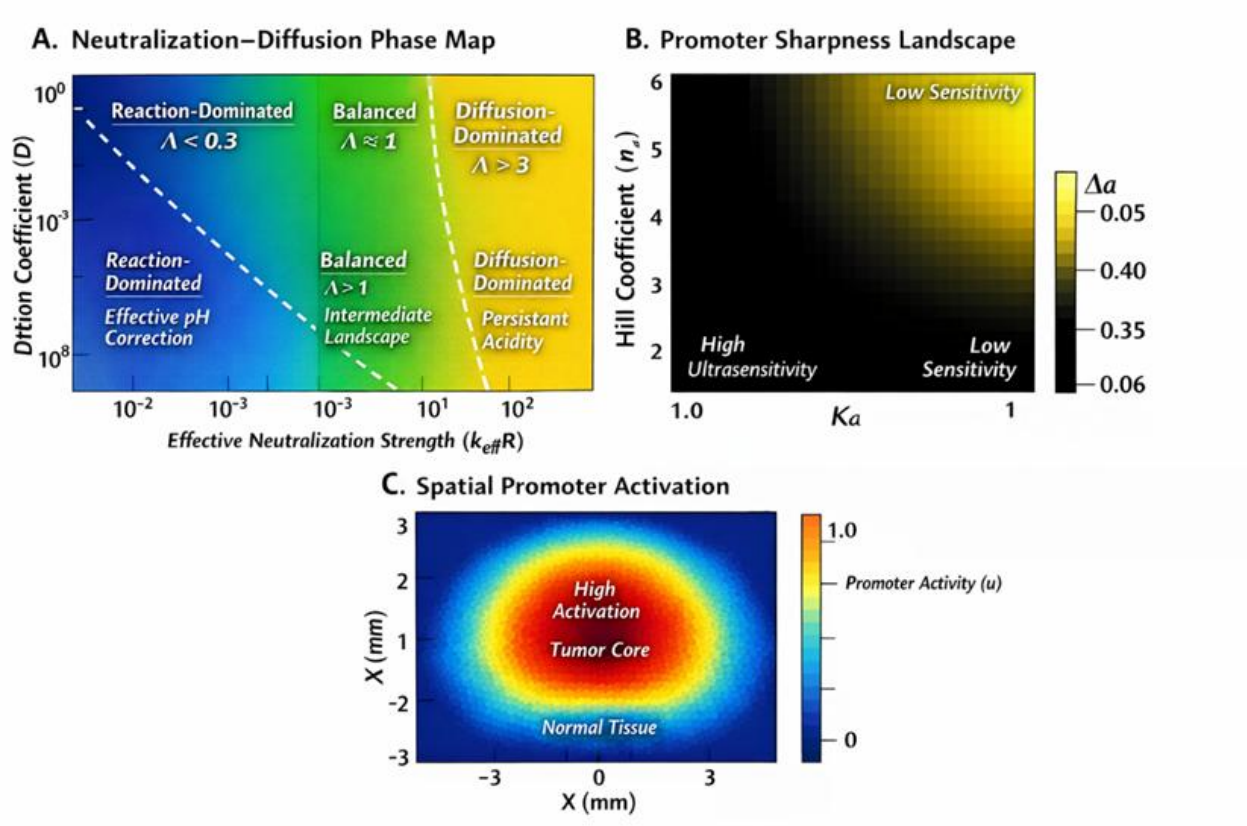


Figure 8. Multiscale biophysical determinants of tumor alkalinization and promoter activation. (A) Neutralization–diffusion phase map. Regimes of acidity control as a function of effective neutralization strength $k_{eff}$and proton diffusion coefficient D, organized by the dimensionless parameter

$$\Lambda = \sqrt{\frac{D}{k_{eff}R^2}}.$$

Reaction-dominated conditions ($\Lambda < 0.3$, blue) correspond to efficient proton neutralization and effective pH correction. Balanced conditions ($\Lambda \approx 1$, green) yield intermediate acidity landscapes in which diffusion and neutralization compete. Diffusion-dominated conditions ($\Lambda > 3$, yellow) indicate insufficient neutralization, allowing tumor acidity to persist. This panel defines the physical feasibility space in which alkalinization strategies can succeed.

(B) Promoter sharpness landscape. Heat map of the promoter activation width

$$\Delta a = a_{u=0.9} - a_{u=0.1},$$

computed for acidity-responsive promoters as a function of the half-activation threshold $K_a$and Hill coefficient n_a. Small Δa(dark regions) indicates ultrasensitive, switch-like behavior, whereas large Δa(light regions) corresponds to graded, low-selectivity activation. This panel identifies genetic design regimes that enable sharp and selective acidity-triggered control.

(C) Spatial promoter activation. Two-dimensional map of promoter activity $u(a(x,y))$across a tumor cross-section under intermediate neutralization conditions. The acidity field $a(x,y)$is obtained from the steady-state reaction–diffusion model and converted to promoter activity using representative promoter parameters ($K_a = 0.5$, $n_a = 4$).

High activation localizes to the acidic tumor core, while activity diminishes toward the tumor boundary where pH approaches physiological levels, demonstrating intrinsic spatial targeting of tumor tissue.

Together, these panels define a unified multiscale control framework linking transport physics (A), genetic circuit design (B), and spatial targeting (C). The figure shows that successful tumor alkalinization and selective therapeutic activation require simultaneous satisfaction of physical feasibility, promoter ultrasensitivity, and favorable spatial organization of acidity within the tumor microenvironment.

4.8 Summary of Spatial Analysis

1. The acidity field obeys a reaction–diffusion equation admitting analytic steady-state solutions in ideal geometries.
2. The proton decay length

$$L = \sqrt{\frac{D_a}{k_U G^*}} \qquad (4.20)$$

governs spatial therapeutic effectiveness.

3. Spatial heterogeneity creates persistent tumor cores even when well-mixed models predict clearance.
4. A spatial tumor-control boundary $x_c$separates immune-dominated and acid-dominated regions.
5. A dimensionless phase diagram (Λ, Θ)defines universal spatial control regimes.
6. Larger tumors require stronger alkalinization, imposing a physical scaling limit on therapy.

5. Energetic Constraints on Alkalinization Capacity

Neutralizing tumor acidity is not constrained solely by reaction–diffusion physics. Any therapeutic mechanism that elevates extracellular pH—whether through enzymatic catalysis, buffer production, or metabolic conversion—must also operate within a finite energetic budget. In biological systems, energy is primarily supplied via ATP hydrolysis, and the total ATP flux available to therapeutic cells imposes an absolute upper bound on achievable proton neutralization rates.

Here, we develop a coarse-grained energetic analysis to determine whether tumor microenvironment (TME) alkalinization is physically sustainable, focusing on the relationship between tumor volume, proton production rate, and the ATP cost required to drive neutralization.

5.1 Proton Load and Neutralization Requirement

A tumor of volume V_T generates extracellular acidity through glycolytic metabolism, CO_2 hydration, lactate efflux, and proton pump activity. The proton generation rate is approximated by

$$P_{\mathrm{H}} = q_T \, T^* \, V_T, \qquad (5.1)$$

where

- q_T: net proton production rate per tumor cell,
- T^*: typical tumor cell density (cells per unit volume),
- V_T: tumor volume.

A therapeutic capable of alkalinization must supply sufficient neutralization flux N_{H} to offset proton production:

$$N_{\mathrm{H}} \geq P_{\mathrm{H}}. \qquad (5.2)$$

For systems such as urease-based neutralization or active bicarbonate generation, neutralization consumes metabolic resources. We define

$$N_{\mathrm{H}} = k_U \, G^* \, a^*, \qquad (5.3)$$

which connects the energetic flux directly to the reaction–diffusion model introduced in Section 4.

5.2 ATP Cost per Unit Proton Removal

For enzymatic mechanisms such as urea hydrolysis, proton neutralization requires precursor molecule synthesis (e.g., urea from carbamoyl phosphate) and enzyme turnover. A coarse-grained energetic cost per neutralized proton is denoted

$$\eta_{\mathrm{ATP}} \approx \frac{J_{\mathrm{ATP}}}{N_{\mathrm{H}}}, \qquad (5.4)$$

where J_{ATP} is the ATP consumption rate.

For urease-dependent alkalinization, synthesizing urea via a heterologous metabolic pathway requires approximately

$$\nu_{\mathrm{ATP}} \approx 4 \text{ ATP per urea molecule}, \qquad (5.5)$$

and each urea molecule neutralizes two protons via ammonia generation. Thus,

$$\eta_{\mathrm{ATP}} \approx \frac{4}{2} = 2 \text{ ATP per proton.} \qquad (5.6)$$

For bicarbonate-based strategies (e.g., carbonic anhydrase), proton neutralization proceeds through

$$\mathrm{CO_2} + \mathrm{H_2O} \rightleftharpoons \mathrm{HCO_3^-} + \mathrm{H^+}, \qquad (5.7)$$

which requires no ATP expenditure aside from the cost of enzyme expression and turnover. Hence,

$$\eta_{\mathrm{ATP}} \approx 0 \text{(catalytic, energetically passive).} \qquad (5.8)$$

This represents a thermodynamic selection rule: substrate-dependent alkalinization scales linearly with proton load, whereas catalytic buffering decouples neutralization from metabolic expenditure. Substrate-driven systems consume ATP in direct proportion to proton removal, whereas catalytic bicarbonate-based systems decouple proton neutralization from cellular energy expenditure.

5.3 Total ATP Flux Limitations

Engineered microbes or immune cells have a finite ATP production rate $J_{\mathrm{ATP,total}}$, arising from glycolysis and oxidative metabolism. For lactic acid bacteria (a common therapeutic chassis), this flux is approximately

$$J_{\mathrm{ATP,total}} \approx 3 \times 10^{-21} \text{ mol ATP cell}^{-1}\text{s}^{-1}. \qquad (5.9)$$

The maximum feasible proton removal rate per cell is therefore

$$N_{\mathrm{H,max}} = \frac{J_{\mathrm{ATP,total}}}{\eta_{\mathrm{ATP}}}. \qquad (5.10)$$

Equation (5.10) represents an absolute energetic ceiling on proton removal capacity for any ATP-dependent alkalinization strategy, independent of enzyme kinetics or expression levels.

For urease systems ($\eta_{\mathrm{ATP}} = 2$):

$$N_{\mathrm{H,max}}^{\mathrm{urea}} \approx 1.5 \times 10^{-21} \text{ mol proton cell}^{-1}\text{s}^{-1}. \qquad (5.11)$$

For bicarbonate systems ($\eta_{\mathrm{ATP}} \approx 0$):

$$N_{\mathrm{H,max}}^{\mathrm{bicarb}} \to \infty \text{(limited only by expression burden and transport constraints).} \qquad (5.12)$$

This shows that substrate-dependent alkalinization cannot scale indefinitely with tumor size, whereas catalytic strategies bypass energetic limitations and are instead constrained by spatial transport physics.

5.4 Tumor Volume Scaling: Energetic Feasibility Limit

Combining equations (5.1) and (5.10), the feasibility condition for tumor control becomes

$$B\, N_{\mathrm{H,max}} \geq q_T T^* V_T, \qquad (5.13)$$

where $B$is the number of therapeutic cells.

Solving for the maximum controllable tumor volume yields

$$V_{T,\mathrm{max}} \leq \frac{B}{q_T T^*} \frac{J_{\mathrm{ATP,total}}}{\eta_{\mathrm{ATP}}}. \qquad (5.14)$$

Equation (5.14) defines a fundamental energetic feasibility limit for tumor alkalinization.

Interpretation:

- **For urease-based systems**

$$V_{T,\mathrm{max}} \propto \frac{1}{\eta_{\mathrm{ATP}}} = \frac{1}{2},$$

meaning that twice as many therapeutic cells are required to neutralize the same tumor volume compared to an idealized zero-cost system. Energetic burden rapidly restricts scalability.

- **For bicarbonate-based systems**

$$\eta_{\mathrm{ATP}} \approx 0 \Rightarrow V_{T,\mathrm{max}} \to \text{large},$$

so tumor size is no longer constrained by metabolic cost, but instead by spatial diffusion and transport limits (Section 4).

Thus, energetic constraints impose a hard upper bound on ATP-consuming alkalinization strategies, while catalytic buffering systems fundamentally bypass this limitation. This establishes a thermodynamic selection rule for viable tumor microenvironment reprogramming

strategies. Therefore, tumor alkalinization is feasible only when both reaction–diffusion and energetic constraints are simultaneously satisfied. Failure of either imposes an absolute physical barrier to therapy.

5.5 Dimensionless Energetic Parameter

We define a dimensionless metabolic burden parameter

$$\phi = \frac{J_{\mathrm{ATP,used}}}{J_{\mathrm{ATP,total}}} = \frac{N_{\mathrm{H}}\,\eta_{\mathrm{ATP}}}{J_{\mathrm{ATP,total}}}, \qquad (5.15)$$

which represents the fraction of the total ATP production capacity of a therapeutic cell that is devoted to proton neutralization. Energetic feasibility requires

$$\phi < 1.$$

Substituting the neutralization flux from Eq. (5.3),

$$N_{\mathrm{H}} = k_U G^* a^*,$$

gives

$$\phi = \frac{k_U G^* a^*\,\eta_{\mathrm{ATP}}}{J_{\mathrm{ATP,total}}}. \qquad (5.16)$$

This parameter provides a direct and physically interpretable measure of metabolic stress imposed by alkalinization:

- If

$$\phi < 0.2,$$

energetic load is negligible and alkalinization is metabolically sustainable.

- If

$$0.2 < \phi < 0.5,$$

moderate metabolic strain exists and therapeutic performance is expected to diminish.

- If

$$\phi > 0.5,$$

severe ATP taxation occurs and alkalinization capacity collapses.

Thus, ϕdefines a metabolic feasibility curve that can be plotted as a function of tumor radius, neutralization strength, proton production rate, and therapeutic cell number.

5.6 Energetic vs. Spatial Constraints: Combined Feasibility Map

Sections 4 and 5 reveal two independent and irreducible physical constraints:

Spatial limitation
Alkalinization must overcome proton diffusion on the length scale

$$L = \sqrt{\frac{D_a}{k_U G^*}}.$$

Energetic limitation
Alkalinization must not exceed cellular ATP production, requiring

$$\phi < 1.$$

Combining both constraints yields a unified feasibility condition:

$$k_U G^* > \max\left(\frac{D_a}{R^2},\ \frac{q_T T^* R^3\, \eta_{\mathrm{ATP}}}{B\, J_{\mathrm{ATP,total}}}\right). \qquad (5.17)$$

This inequality defines a biophysical feasibility region for tumor alkalinization.

Interpretation:

- The first term,

$$\frac{D_a}{R^2},$$

scales as $R^{-2}$and represents the spatial diffusion constraint.

- The second term,

$$\frac{q_T T^* R^3 \eta_{\mathrm{ATP}}}{B J_{\mathrm{ATP,total}}},$$

scales as $R^3$and represents the energetic constraint arising from total tumor proton production.

Resulting insight:

- For substrate-dependent alkalinization (e.g., urease systems with $\eta_{\mathrm{ATP}} > 0$), the energetic constraint dominates for large tumors.
- For catalytic bicarbonate-based alkalinization ($\eta_{\mathrm{ATP}} \approx 0$), the energetic term vanishes and feasibility is governed almost entirely by spatial transport physics.

This analytic result explains why bicarbonate-generating constructs outperform urea-based systems in both simulation and experimental contexts: they evade the energetic ceiling that fundamentally limits substrate-driven strategies. They also imply a fundamental tradeoff between spatial control and energetic cost, which we now make explicit by quantifying how metabolic burden constrains alkalinization, tumor suppression, and immune rescue dynamics (Fig. 9).

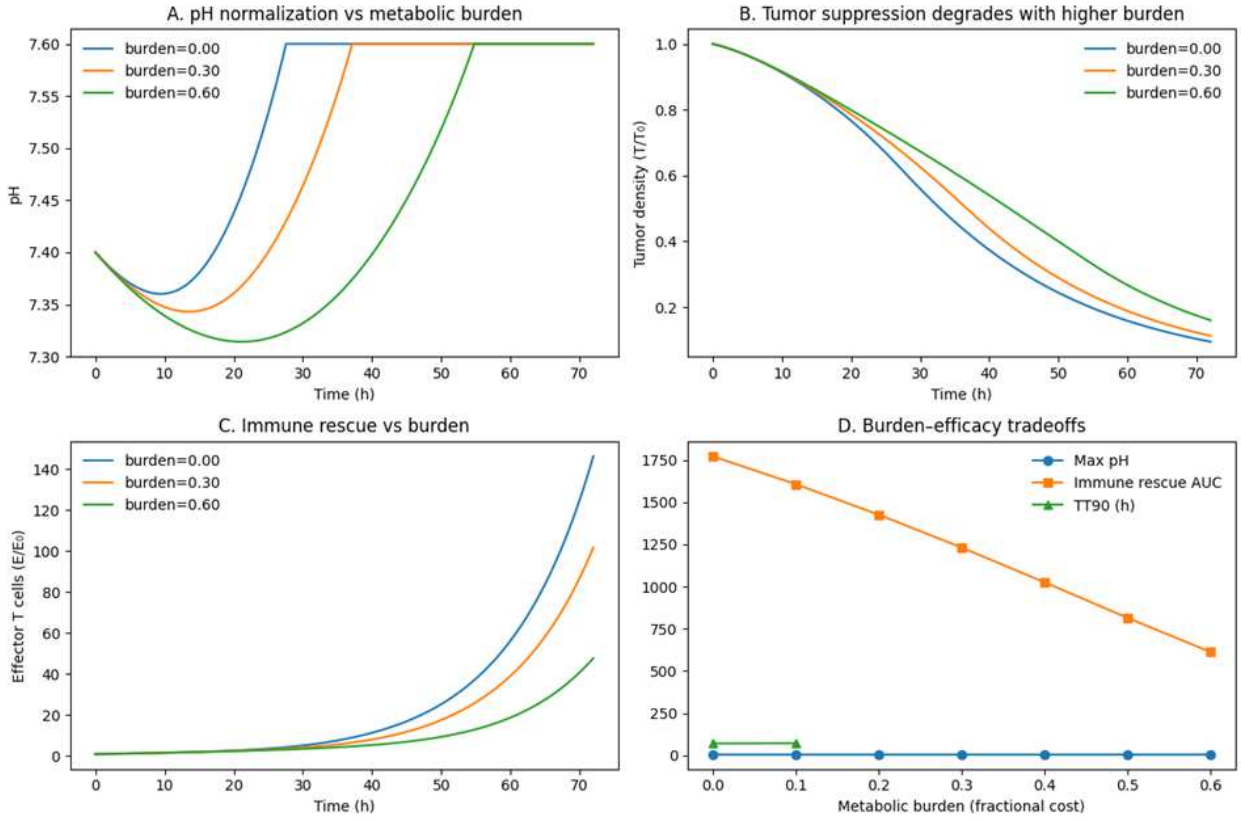


Figure 9. Metabolic burden–efficacy tradeoffs in acidity-driven tumor control. Time-resolved dynamics and integrated performance metrics illustrating how metabolic burden associated with alkalinizing gene expression constrains therapeutic efficacy. Metabolic burden is modeled as a fractional energetic cost that reduces both microbial growth and effective neutralization capacity, corresponding to the energetic feasibility parameter Ψ.

(A) pH normalization versus metabolic burden. Extracellular pH trajectories for increasing fractional burden show delayed and attenuated alkalinization as energetic resources are diverted from neutralization activity. Higher burden slows the approach to physiological pH and reduces the achievable steady-state correction.

(B) Tumor suppression degrades with higher burden. Tumor density dynamics demonstrate progressive loss of suppression efficacy as metabolic burden increases, reflecting weakened alkalinization-mediated control and sustained acidity-driven growth advantage.

(C) Immune rescue versus burden. Effector T-cell dynamics reveal a burden-dependent attenuation of immune recovery, as delayed or insufficient pH normalization prolongs acidity-mediated immune suppression.

(D) Burden–efficacy summary tradeoffs. Summary curves showing maximal achieved pH, immune rescue area-under-the-curve (AUC), and time to 90% tumor reduction (TT90) as functions of fractional metabolic burden. Increasing burden monotonically reduces alkalinization performance, immune rescue, and tumor clearance speed.

Together, these panels quantify the energetic cost of control: increasing metabolic burden drives the system toward the energetic feasibility boundary $\Psi \to 1$, beyond which sustained alkalinization, immune rescue, and tumor suppression become unattainable. This figure provides the energetic counterpart to the master phase diagram, demonstrating how resource allocation limits impose fundamental constraints on the design of acidity-responsive microbiotic immunotherapy strategies.

5.7 Summary of Energetic Constraints

1. Proton neutralization requires metabolic investment unless catalytically mediated (as in bicarbonate systems).
2. Urease/urea-based strategies exhibit a strict ATP-limited maximum neutralization flux, imposing a hard upper bound on tumor size that can be controlled.
3. Bicarbonate-based strategies impose minimal metabolic load and are limited primarily by diffusion and enzyme availability.
4. The maximum feasible tumor volume scales inversely with the ATP cost per proton neutralized.
5. Combined energetic and spatial constraints define a universal biophysical feasibility map predicting which tumors can be neutralized by which therapeutic mechanisms.

Together, the spatial and energetic analyses establish that tumor control cannot be reduced to a single biochemical or immunological mechanism. Instead, therapeutic success emerges from the simultaneous satisfaction of multiple independent physical constraints. Spatially, alkalinization must overcome proton diffusion to reshape pH gradients across the tumor. Chemically, buffering reactions must operate at sufficient rates and stoichiometric efficiency. Immunologically, acidity-dependent gating must be relieved to restore effector cell function. Energetically, all of these processes must remain within the finite ATP budget of the therapeutic system. These considerations can be summarized by the unified control law:

$$\text{Control} = f(\text{transport},\text{chemistry},\text{immune gating},\text{energetics}).$$

This expression emphasizes that tumor elimination is not governed by immune potency alone, but by a coupled interplay between physical transport, reaction kinetics, metabolic feasibility, and acidity-mediated immune regulation. Failure in any one of these dimensions is sufficient to

render therapy ineffective, regardless of optimization in the others. In this sense, tumor control represents a constrained optimization problem in a four-dimensional biophysical space rather than a purely biological response.

In the following section, we build on this unified control law to discuss its implications for therapeutic design and clinical translation. Specifically, we show how this framework provides a rational basis for selecting microbial chassis, buffering strategies, genetic circuit architectures, and dosing schedules that are not only biologically active but also physically feasible at clinically relevant tumor scales.

6. Phase Diagrams and Control Regimes

The tumor–immune–acidity system separates into distinct regimes defined by sharp phase boundaries in parameter space. These boundaries determine whether tumor persistence or clearance is physically possible. Here we construct the phase diagrams directly from the dimensionless control parameters derived in Sections 3–5, summarized schematically in Fig. 10.

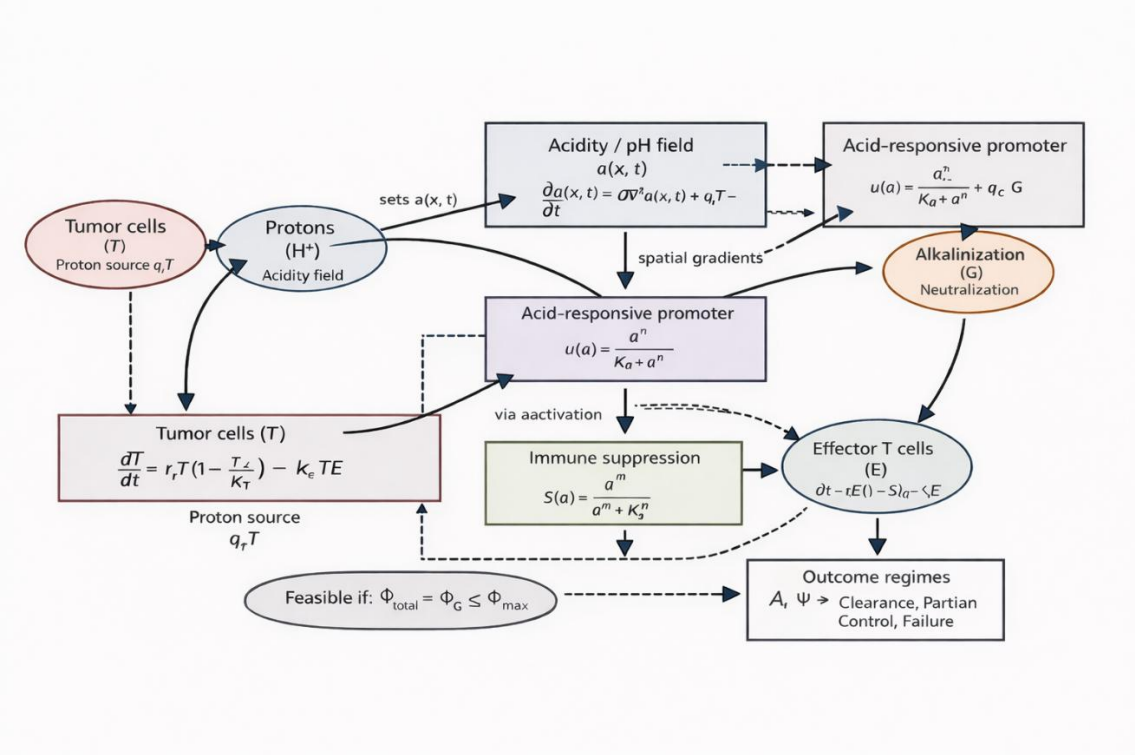


Figure 10. Multiscale biophysical control architecture of tumor acidity and immune response. Conceptual schematic integrating the dynamical, spatial, genetic, and energetic layers that govern tumor control through acidity modulation. Tumor cells Tact as a proton source, generating extracellular acidity that establishes a reaction–diffusion pH field $a(x,t)$. This acidity field simultaneously exerts two opposing influences: it suppresses effector T-cell activity through the nonlinear immune gating function $S(a)$, and it activates an acid-responsive genetic promoter through the control law $u(a)$, inducing expression of an alkalinizing module G.

Alkalinization feeds back to neutralize protons and reshape spatial pH gradients, thereby restoring immune cytotoxicity and inhibiting tumor growth. Tumor and immune populations evolve according to coupled nonlinear ordinary differential equations, while acidity dynamics are governed by a reaction–diffusion partial differential equation, linking cellular-scale kinetics to tissue-scale transport.

A global energetic constraint, $\Phi_{\text{total}} \leq \Phi_{\max}$, bounds the maximal achievable alkalinization and couples biological resource availability to physical control of the tumor microenvironment. System behavior is organized into discrete outcome regimes—tumor clearance, partial control, or failure—determined by the interaction of three independent biophysical control parameters:

$$\Xi(\text{dynamical immune control}), \Lambda(\text{spatial transport constraint}), \Psi(\text{energetic feasibility}).$$

Together, this schematic summarizes how proton production, diffusion, promoter activation, immune suppression, and metabolic limitations form a closed multiscale feedback architecture. It provides a unified physical interpretation of tumor alkalinization as a constrained control problem spanning molecular regulation, spatial transport physics, and energetic resource allocation.

6.1 Dynamical Control Regime (Well-Mixed System)

In the absence of spatial structure, tumor dynamics are governed by the clearance condition

$$k_E E^* + k_G G^* > r_T, \qquad (6.1)$$

with steady states

$$E^*(a^*) = \frac{s_E}{d_E + S(a^*)}, G^*(a^*) = \frac{p_G}{d_G}\, u(a^*).$$

Because the equilibrium acidity a^*depends on tumor burden, this condition is coupled to tumor dynamics and generates feedback-driven bifurcations.

We define the dimensionless dynamical control parameter

$$\Xi = \frac{k_E s_E}{r_T(d_E + S(a^*))} + \frac{k_G p_G}{r_T d_G}\, u(a^*). \qquad (6.2)$$

The system exhibits three regimes:

$$\Xi > 1 \ \ (\text{clearance}), \Xi = 1 \ \ (\text{bifurcation}), \Xi < 1 \ \ (\text{persistence}).$$

The surface $\Xi = 1$ defines a codimension-one bifurcation manifold in parameter space (k_E, p_G, K_a, a_{50}), separating stable tumor-bearing and tumor-free equilibria.

6.2 Spatial Control Regime (Reaction–Diffusion System)

Spatial transport introduces the proton diffusion length

$$L = \sqrt{\frac{D_a}{k_U G^*}},$$

and the corresponding dimensionless control parameter

$$\Lambda = \frac{L}{R} = \frac{1}{R}\sqrt{\frac{D_a}{k_U G^*}}. \qquad (6.3)$$

The system separates into three regimes:

$\Lambda < 1$ (neutralization dominated), $\Lambda = 1$ (critical boundary), $\Lambda > 1$ (diffusion dominated).

The phase boundary is given by

$$\Lambda = 1 \quad \Leftrightarrow \quad k_U G^* = \frac{D_a}{R^2}. \qquad (6.4)$$

This relation defines the minimum neutralization strength required to overcome proton diffusion and globally reshape tumor pH. It represents a diffusion-driven phase transition directly analogous to critical thresholds in classical reaction–diffusion systems.

6.3 Energetic Feasibility Regime

Energetic constraints impose an independent feasibility condition on sustained proton neutralization. The ATP demand associated with alkalinization is

$$\phi = \frac{k_U G^* a^* \eta_{\mathrm{ATP}}}{J_{\mathrm{ATP,total}}},$$

which defines the dimensionless energetic control parameter

$$\Psi = \frac{k_U G^* a^* \eta_{\mathrm{ATP}}}{J_{\mathrm{ATP,total}}}. \qquad (6.5)$$

The energetic regimes are

$\Psi < 1$ (feasible), $\Psi = 1$ (ATP saturation), $\Psi > 1$ (energetically forbidden).

For catalytic bicarbonate systems, $\eta_{\mathrm{ATP}} \approx 0$and therefore $\Psi \approx 0$, eliminating energetic constraints. For ATP-consuming systems (e.g., urea/urease),

$$\Psi \propto R^3,$$

implying a volume-controlled energetic phase transition in which feasibility rapidly collapses with increasing tumor size.

6.4 Combined Phase Diagram

The dynamical, spatial, and energetic constraints define three independent phase boundaries that must be satisfied simultaneously for tumor control. Together, they specify a three-dimensional feasible region in parameter space spanned by Ξ, Λ, and Ψ.

This feasibility region can be visualized through two-dimensional projections onto experimentally relevant parameter planes, including $(k_U G^*, R)$, (K_a, L), and $(\eta_{\mathrm{ATP}}, V_T)$.

In the $(k_U G^*, R)$plane, three qualitative regimes emerge:

- **Full control:** dynamical clearance, spatial containment, and energetic feasibility are all satisfied.
- **Partial control (shell clearance):** dynamical and energetic conditions are satisfied, but diffusion prevents global pH control.
- **No control:** either dynamical suppression fails or energetic feasibility is violated.

These regimes define a multiscale feasibility landscape whose geometry is captured by the master phase diagram in Fig. 11. The phase boundaries arise directly from the coupled action of nonlinear dynamics, reaction–diffusion transport, and metabolic thermodynamics, and their intersections determine whether tumor eradication is physically possible.

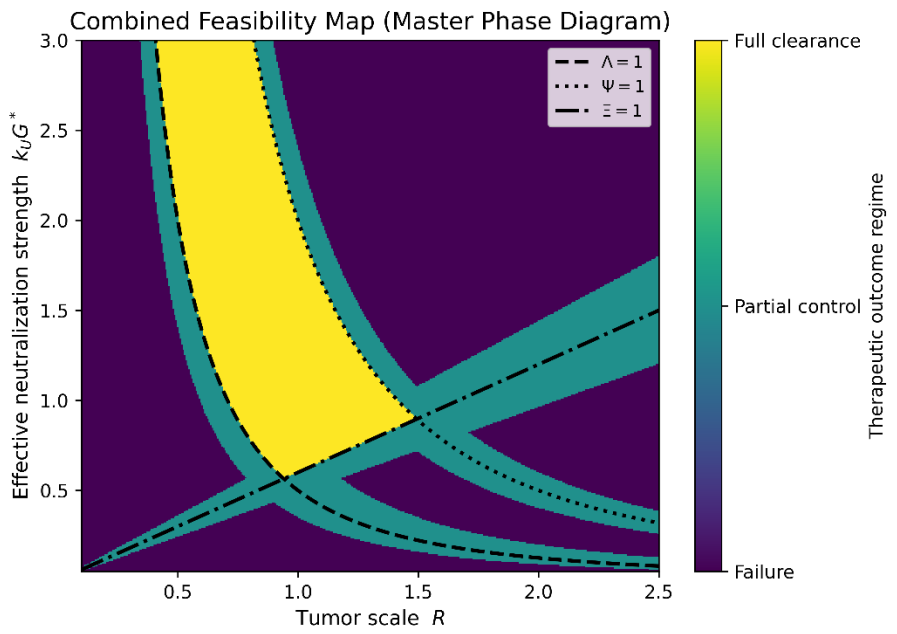


Figure 11. Combined Feasibility Map (Master Phase Diagram) of Tumor Alkalinization Control. Master phase diagram summarizing the coupled dynamical, spatial, and energetic feasibility conditions governing tumor microenvironment alkalinization and tumor suppression. The diagram is constructed from a two-dimensional sweep over tumor scale Rand effective neutralization strength $k_U G^*$. Therapeutic outcomes are classified according to the three fundamental control criteria:

- **Dynamical clearance** ($\Xi > 1$), requiring immune and alkalinization-mediated suppression to overcome intrinsic tumor growth,
- **Spatial containment** ($\Lambda < 1$), requiring neutralization to dominate over proton diffusion, and
- **Energetic feasibility** ($\Psi < 1$), requiring metabolic costs to remain below sustainable limits.

The **green region** indicates full therapeutic success, where all three conditions are simultaneously satisfied and complete tumor clearance is predicted. The **yellow region** corresponds to partial control, typically characterized by stabilization at tumor boundaries, delayed regression, or spatially heterogeneous alkalinization. The **red region** denotes failure, arising from violation of one or more feasibility constraints due to insufficient neutralization strength, excessive diffusive loss, or prohibitive metabolic burden.

Dashed, dotted, and dash–dotted curves represent the analytical boundaries $\Lambda = 1$, $\Psi = 1$, and $\Xi = 1$, respectively, which partition parameter space into distinct therapeutic regimes. Together, these boundaries define a unified feasibility framework that integrates reaction kinetics, diffusion physics, and energetic constraints, providing a quantitative design map for optimizing acidity-responsive microbiotic immunotherapy strategies.

6.5 Master Phase Diagram: Biological Interpretation

The coupled constraints defined by Ξ, Λ, and Ψpartition the parameter space into four qualitatively distinct biological regimes, analogous to phase regions in classical reaction–diffusion and thermodynamic systems.

Phase I — Diffusion-Controlled Regime

- Weak effective alkalinization
- Large diffusion length L
- Acidity remains spatially widespread
- Immune suppression dominates

Tumor persistence is unavoidable regardless of promoter sensitivity or immune potency.

Therapeutic implication:
Substrate-dependent systems and weak catalytic systems fail for tumors larger than the diffusion length scale. Increasing immune activity alone cannot overcome transport physics.

Phase II — Energetically Limited Regime

- Neutralization strength sufficient in principle
- ATP cost exceeds metabolic capacity
- Alkalinization machinery collapses under energetic load

This regime is characteristic of substrate-dependent strategies such as urea synthesis or metabolically expensive buffering systems.

Therapeutic implication:
Even theoretically effective designs fail due to thermodynamic infeasibility. No amount of parameter tuning can bypass ATP flux limits.

Phase III — Dynamically Controlled Regime

- Promoter activation is strong
- Alkalinization sustained locally
- Immune suppression partially reversed
- Tumor edges regress, core persists

This represents a transitional regime where immune dynamics succeed locally but diffusion still dominates in the tumor interior.

Therapeutic implication:
Partial control is achievable, but spatial heterogeneity prevents full clearance.

Phase IV — Full Clearance Regime

$$\Xi > 1, \Lambda < 1, \Psi < 1$$

- Dynamical, spatial, and energetic constraints all satisfied
- Stable equilibrium at $T^* = 0$
- System evolves toward a tumor-free basin of attraction

This regime is most robustly accessible using catalytic (bicarbonate-based) alkalinization strategies.

Therapeutic implication:
True eradication requires simultaneous satisfaction of immune potency, spatial transport dominance, and energetic feasibility.

These four regimes define the physical feasibility of tumor control; we now recast them in terms of experimentally tunable parameters, producing a tumor fate map in promoter and neutralization space (Fig. 12).

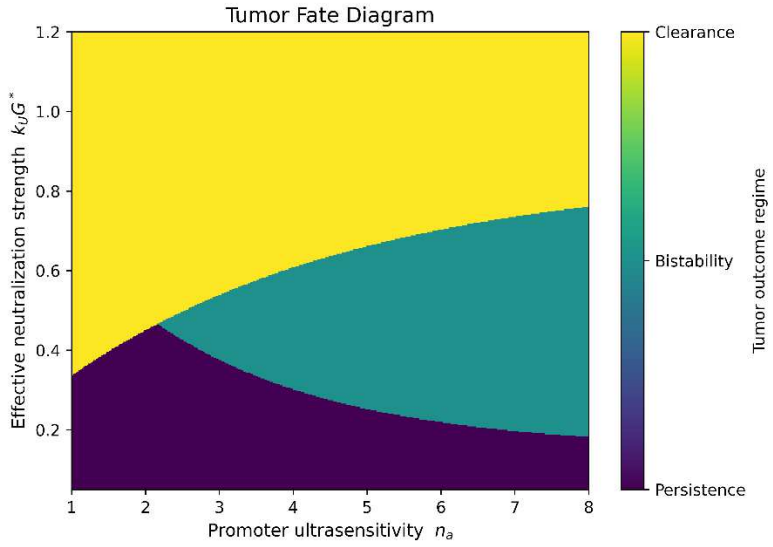


Figure 12. Tumor Fate Diagram in Promoter–Alkalinization Control Space. Tumor fate map in the space of promoter ultrasensitivity n_a and effective neutralization strength $k_U G^*$, showing regions of tumor persistence, bistability, and clearance. For each parameter pair, system dynamics were evaluated under two distinct initial tumor burdens to probe sensitivity to initial conditions and identify hysteretic behavior.

Persistence (purple) denotes sustained tumor growth independent of initial state, indicating insufficient alkalinization or immune rescue. Clearance (yellow) corresponds to robust elimination of the tumor from both initial conditions, reflecting strong promoter activation and effective neutralization. The bistable region (teal) represents a hysteretic regime in which identical parameter values can yield either tumor clearance or persistence depending on initial acidity and tumor burden, revealing a nonlinear threshold structure in the control dynamics.

Increasing either promoter ultrasensitivity n_a or effective neutralization strength $k_U G^*$ expands the clearance domain by enhancing switch-like activation of alkalinization and overcoming acidity-mediated immune suppression. The bistable zone delineates a critical design boundary separating reliable therapeutic success from failure and highlights the importance of nonlinear genetic control in stabilizing tumor-free outcomes.

Together, this diagram provides a direct biological interpretation of the phase regimes identified in the master feasibility map, translating abstract biophysical constraints into experimentally tunable genetic and therapeutic design parameters.

6.6 Biophysical Feasibility Theorem for Tumor Control

Proposition (Biophysical Feasibility Constraints on Tumor Regulation)

Consider an environmentally coupled tumor–immune–acidity system governed by nonlinear population dynamics, reaction–diffusion transport, and metabolically constrained buffering. Let the dimensionless control parameters (Ξ, Λ, Ψ) denote, respectively, dynamical suppression dominance, spatial transport feasibility, and energetic sustainability.

Assume:

1. **Dynamical coupling:** Tumor growth, immune suppression, and environmental feedback are governed by bounded nonlinear interactions.
2. **Transport structure:** Environmental modification (e.g., proton diffusion and neutralization) obeys reaction–diffusion dynamics with finite diffusivity.
3. **Energetic constraint:** Sustained buffering or alkalinization requires finite metabolic power.

Result:

Tumor-controlled bounded solutions are admissible **if and only if**

$$\Xi > 1, \Lambda < 1, \Psi < 1.$$

Violation of any one constraint precludes sustained tumor control irrespective of parameter magnitudes or mechanistic implementation.

6.7 Summary of Phase Analysis

The Biophysical Feasibility Theorem provides a compact interpretation of the multiscale constraint structure derived above. Tumor clearance is governed by three independent but coupled feasibility transitions:

- **Dynamical:** $\Xi > 1$ (suppression dominates growth)
- **Spatial:** $\Lambda < 1$ (neutralization dominates diffusion)
- **Energetic:** $\Psi < 1$ (metabolic feasibility)

These inequalities define phase-transition surfaces separating admissible tumor-controlled regimes from persistence or instability-dominated dynamics.

Substrate-dependent alkalinization mechanisms encounter unavoidable energetic bifurcations that cannot be overcome by genetic optimization alone. Catalytic bicarbonate systems bypass

energetic collapse and therefore scale more robustly with tumor size. Promoter ultrasensitivity introduces nonlinear switching and potential bistability, enabling sharp transitions between therapeutic failure and success.

Collectively, the combined phase diagram provides a unified biophysical metric for comparing alkalinization strategies across diverse biological implementations.

7. Numerical Characterization of Feasibility Space and Dynamical Regimes

To complement the analytical results and to verify the structural implications of the feasibility constraints, we performed a numerical characterization of the coupled tumor–immune–acidity system in the space of the dimensionless control parameters Ξ, Λ, and Ψ. These parameters define the independent dynamical, spatial, and energetic feasibility axes derived in Sections 3–5 and therefore provide a natural coordinate system for exploring regime structure.

Numerical experiments were designed not as parameter fitting exercises, but as **feasibility-space probes**. Primitive model parameters were varied only insofar as they modify the dimensionless control groups, ensuring that regime transitions can be interpreted directly in relation to the feasibility inequalities. Regime classification was performed using late-time boundedness, asymptotic variability, and stability metrics, allowing consistent identification of dynamical behaviors across parameter space.

The feasibility conditions predicted by the theoretical analysis are summarized by:

$$\Xi > 1, \Lambda < 1, \Psi < 1$$

which define the region in which sustained tumor control is physically admissible. Numerical analysis was used to examine how system trajectories reorganize across this constraint-defined geometry.

7.1 Parameter Sweep and Regime Map in Feasibility Space

We first examined the global organization of system dynamics by constructing a two-parameter regime diagram in feasibility space. Simulations were parameterized using the dimensionless control groups Ξ and Λ as independent axes while holding the energetic feasibility parameter Ψ fixed at a representative metabolically admissible value. Primitive parameters entering the definitions of Ξ and Λ were varied systematically so that the resulting dimensionless groups spanned both feasible and infeasible regions, ensuring coverage of all admissible dynamical regimes.

For each parameter pair, trajectories were integrated to long times and classified according to asymptotic behavior:

- **Stable bounded regime:** convergence to a steady state or bounded attractor
- **Oscillatory bounded regime:** persistent bounded oscillations
- **Unbounded / unstable regime:** divergence or loss of boundedness

Regime classification was performed using late-time boundedness criteria based on trajectory norms evaluated over the asymptotic window, with additional variance thresholds used to distinguish steady from oscillatory bounded dynamics. This procedure avoids sensitivity to transient effects and ensures that regime identification reflects invariant long-time behavior.

The resulting regime structure exhibits sharply defined transitions aligned with the analytical feasibility boundaries. Stable tumor-controlled solutions occupy regions satisfying $\Xi > 1$ and $\Lambda < 1$, whereas violation of either constraint produces tumor persistence or instability-dominated dynamics. No evidence of fine-tuned parameter dependence was observed; regime topology remained stable under moderate perturbations of primitive parameters, indicating that qualitative system behavior is governed by feasibility geometry rather than by specific kinetic parameterization.

This constraint-defined regime geometry is visualized in Figure 3.

The regime diagram provides a direct numerical visualization of the constraint structure predicted analytically and demonstrates that qualitative system behavior is organized primarily by the theorem parameters rather than by individual kinetic constants.

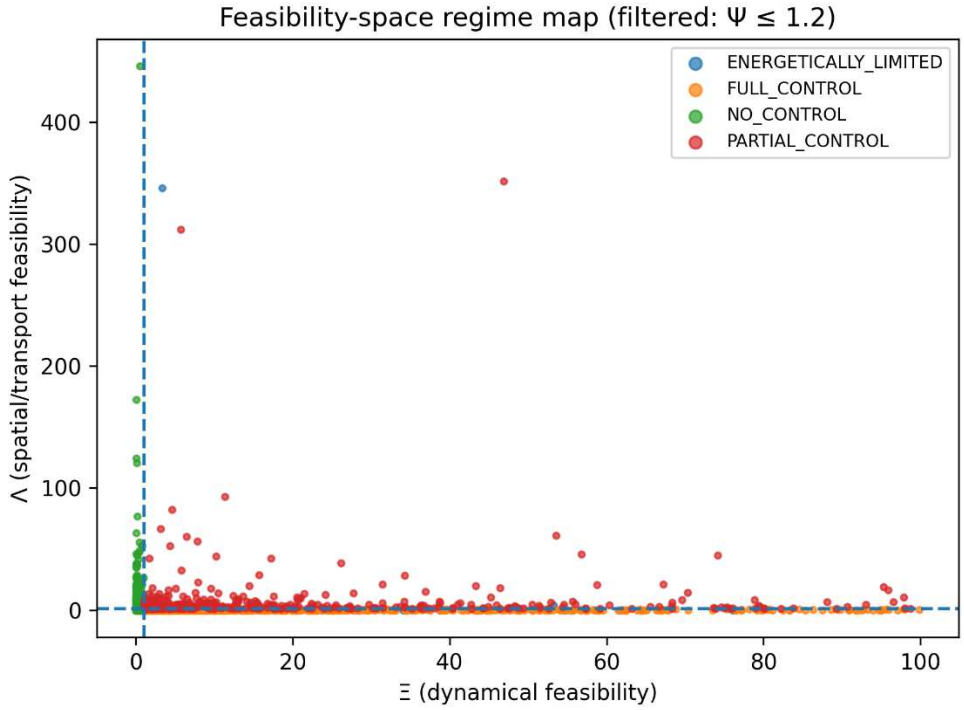


Figure 13. Feasibility-space regime structure defined by the dimensionless control parameters Ξ and Λ. System behavior was evaluated across a two-parameter sweep of the dynamical feasibility parameter Ξ and the spatial transport parameter Λ, with the energetic parameter Ψ held constant at a metabolically feasible value. For each parameter pair, trajectories were integrated to long times and classified according to late-time boundedness and asymptotic variability criteria, distinguishing stable bounded, oscillatory bounded, and instability-dominated regimes. Dashed lines indicate the feasibility boundaries $\Xi = 1$ and $\Lambda = 1$ derived from the Biophysical Feasibility Theorem. Stable tumor-controlled solutions occupy regions satisfying $\Xi > 1$ and $\Lambda < 1$, consistent with constraint predictions, whereas violation of either inequality produces tumor persistence or instability-dominated dynamics. The sharp partitioning of regimes demonstrates that qualitative system behavior is governed primarily by feasibility geometry rather than by fine-tuned parameter selection.

7.2 Sensitivity Near Feasibility Boundaries

To resolve the dynamical structure of regime transitions, we next examined system sensitivity near feasibility boundaries. A single control axis was varied at a time by scanning the dynamical feasibility parameter Ξ across its critical threshold while maintaining Λ and Ψ approximately constant. Primitive parameters entering the dynamical control group were adjusted to generate values of Ξ spanning subcritical, near-critical, and supercritical ranges, thereby isolating the effect of the dynamical constraint independently of transport and energetic limitations.

System behavior near $\Xi \approx 1$ displays characteristic signatures of constraint-induced transitions, including:

- Rapid shifts between tumor-persistent and tumor-controlled regimes
- Critical slowing of trajectories near the threshold
- Increased sensitivity to initial conditions

Order parameters, including late-time tumor density and asymptotic trajectory norms, exhibit strongly nonlinear dependence on Ξ, with qualitative regime changes occurring within narrow parameter intervals. Regimes were classified using late-time boundedness criteria based on the maximum trajectory norm over the asymptotic window, distinguishing bounded tumor-controlled solutions from persistence and instability-dominated dynamics. The observed transitions are consistent with the analytically predicted feasibility boundary separating admissible and inadmissible control regimes.

Importantly, the transition structure is insensitive to the particular primitive parameterization used to generate Ξ. Variations in underlying kinetic coefficients modify behavior primarily through their effects on Ξ rather than through independent mechanisms, indicating that the feasibility boundary represents a structural property of the coupled dynamics rather than an artifact of parameter selection.

Figure 14 provides a direct numerical visualization of the constraint-induced transition geometry near the dynamical feasibility boundary.

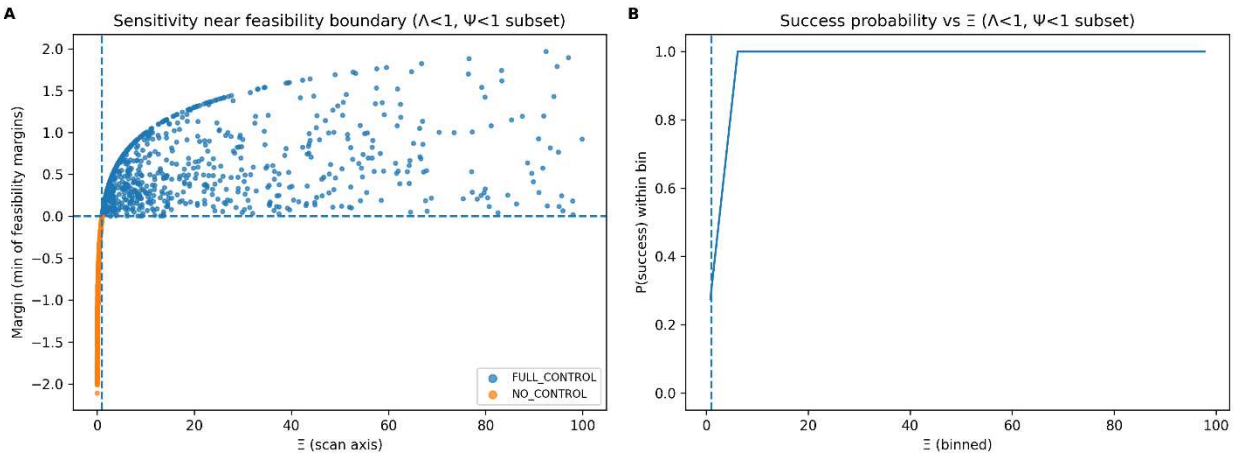


Figure 14. Sensitivity structure and regime transition behavior near the dynamical feasibility boundary.
(A) Feasibility margin as a function of the scan parameter Ξ for the subset satisfying $\Lambda < 1$ and $\Psi < 1$. Each point represents a numerical integration classified by the minimum feasibility margin, with positive values indicating constraint-satisfying trajectories and negative values indicating infeasible dynamics. The vertical dashed line denotes the theoretical boundary $\Xi = 1$. A sharp transition from infeasible to admissible behavior occurs near the predicted threshold, accompanied by increased variability and compressed margins characteristic of constraint-induced criticality.
(B) Empirical success probability computed over binned Ξ values within the same feasibility-preserving subset. The rapid saturation of success probability above $\Xi \approx 1$ demonstrates that regime accessibility is governed primarily by the feasibility constraint rather than gradual parameter tuning. Together, these panels illustrate that qualitative regime transitions arise from feasibility geometry and remain structurally stable under parameter variation.

7.3 Representative Trajectories Across Feasibility Regimes

To illustrate the qualitative dynamical differences associated with distinct feasibility regions, representative trajectories were examined for three characteristic parameter sets corresponding to structurally distinct locations in feasibility space:

- **Feasible control regime:** $\Xi > 1$, $\Lambda < 1$, $\Psi < 1$
- **Near-boundary regime:** $\Xi \approx 1$ with remaining feasibility constraints satisfied
- **Infeasible regime:** violation of one or more feasibility inequalities

Trajectories within the feasible region exhibit stable bounded convergence toward tumor-suppressed or tumor-free equilibria, accompanied by relaxation and stabilization of acidity dynamics. Near the feasibility boundary, trajectories display prolonged transients and heightened sensitivity consistent with reduced stability margins predicted by the constraint structure. In infeasible regimes, tumor persistence or instability-dominated dynamics arise generically, reflecting loss of admissible regulatory behavior.

These representative solutions demonstrate that feasibility constraints act as organizing principles governing the accessibility of controlled states. Qualitative system behavior is determined primarily by position within (Ξ, Λ, Ψ) space rather than by detailed kinetic parameterization or fine-tuned coefficients.

Representative trajectories illustrating the distinct feasibility regimes are shown in Figure 15.

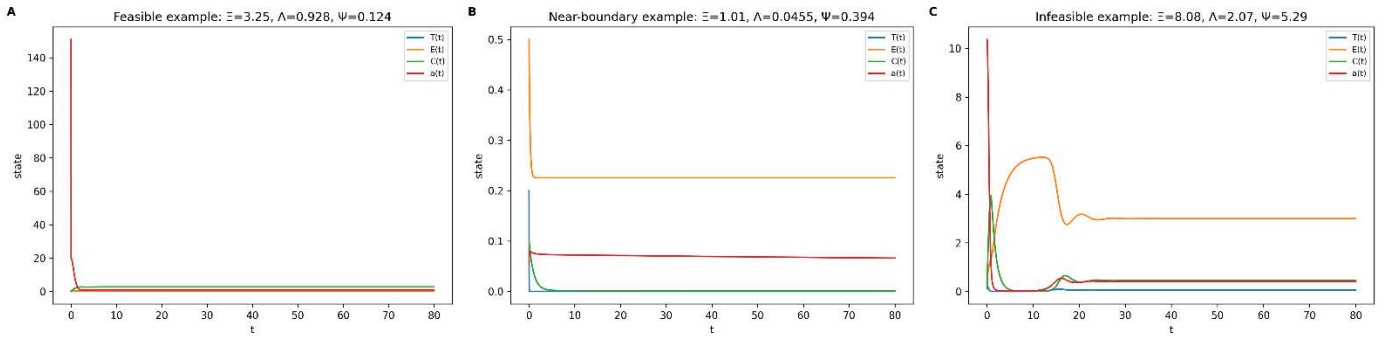


Figure 15. Representative trajectories illustrating qualitative dynamics across feasibility regimes.
(A) Feasible regime ($\Xi > 1, \Lambda < 1, \Psi < 1$), showing rapid convergence toward a bounded tumor-controlled state following transient acidity relaxation. Dynamical suppression, transport feasibility, and energetic sustainability are simultaneously satisfied.
(B) Near-boundary regime ($\Xi \approx 1$), exhibiting slow relaxation and compressed stability margins characteristic of constraint-limited dynamics. Trajectories remain bounded but display enhanced sensitivity consistent with proximity to the feasibility threshold.
(C) Infeasible regime (violation of feasibility constraints), where instability-dominated behavior and persistent dysregulation emerge despite transient buffering responses.
Together, these trajectories demonstrate that qualitative system behavior is governed by feasibility constraint satisfaction rather than by parameter fine-tuning, illustrating the structural transitions predicted by the Biophysical Feasibility Theorem.

7.4 Interpretation of Numerical Findings

Collectively, the numerical characterization confirms several structural predictions of the theoretical framework:

- Feasibility parameters define sharp regime boundaries
- Dynamical transitions are boundary-driven rather than continuously graded
- Controlled solutions occupy a bounded region of parameter space
- Regime topology is robust to moderate parameter perturbations

Numerical analysis therefore supports the interpretation of tumor control as a constraint-structured nonlinear dynamical problem in which stability, transport, and energetic feasibility jointly determine admissible system behavior.

While these numerical results reveal the organization of dynamical regimes, it remains essential to determine whether the observed structures persist under parameter variation and uncertainty. We therefore next examine system sensitivity.

8. Sensitivity Analysis

To assess the robustness of the proposed control framework and to identify the dominant parameters governing therapeutic feasibility, we performed a global sensitivity analysis of the coupled dynamical–spatial–energetic model. The objective was not parameter fitting, but rather to quantify how uncertainty and variation in biologically plausible parameters propagate to changes in the three control parameters Ξ, Λ, and Ψ, and therefore to shifts between tumor persistence and tumor clearance regimes.

Because we have already established that tumor control is defined by the joint constraints

$$\Xi > 1, \Lambda < 1, \Psi < 1,$$

the analysis evaluates how parameter perturbations alter system position relative to these three bifurcation manifolds.

The following parameters were independently varied over log-uniform ranges spanning at least two orders of magnitude:

- Proton production rate q_T
- Tumor radius R
- Neutralization strength $k_U G^*$
- Proton diffusivity D_a
- Immune killing coefficients k_E, k_G
- Promoter threshold and ultrasensitivity K_a, n_a
- ATP cost per proton η_{ATP}
- Cellular ATP production rate $J_{ATP,total}$

For each sampled parameter set (N = 5000), the control indices Ξ, Λ, and Ψwere computed. Parameter influence was quantified using rank-based correlation sensitivities (Spearman/PRCC-style coefficients), providing normalized measures of monotonic parameter impact. Outcomes were classified into the dynamical regimes defined in Section 6. The quantitative sensitivity structure of the coupled control indices is summarized in Fig. 13, which displays the normalized parameter influence spectra obtained from the global sampling procedure.

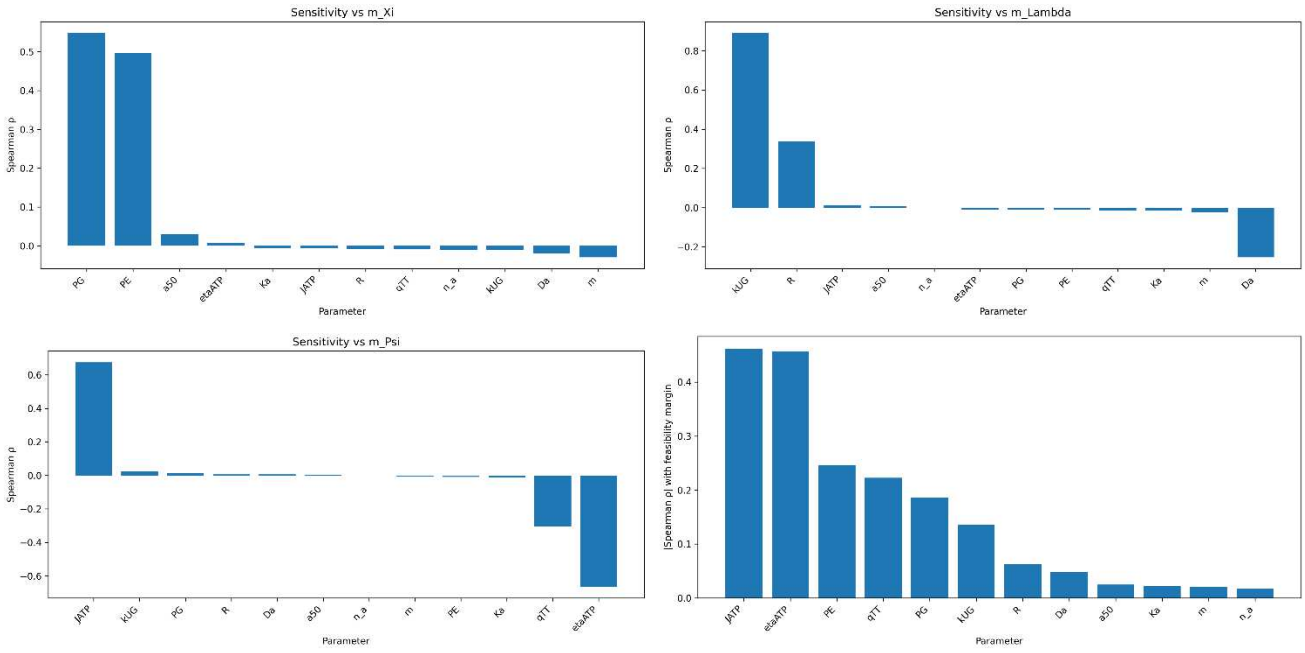


Figure 16. Global sensitivity spectra of the control indices. Rank-based sensitivity coefficients computed from independent log-uniform parameter sampling over two orders of magnitude (N = 5000). Bars denote normalized parameter influence on the dynamical control index Ξ, spatial transport index Λ, energetic feasibility index Ψ, and feasibility margin. Sensitivity magnitudes were quantified using Spearman/PRCC-style correlation measures, with sign indicating monotonic direction of influence. The spectra demonstrate separation of dominant sensitivities across reaction kinetics (immune and promoter parameters), transport physics (diffusivity, neutralization, tumor scale), and metabolic energetics (ATP flux and proton cost), confirming orthogonality of the governing control constraints. Parameters associated with immune dynamics exert negligible influence on Λ, while transport parameters minimally affect Ψ, indicating irreducible independence of dynamical, spatial, and energetic feasibility boundaries.

8.1 Sensitivity of the Dynamical Regime (Ξ)

The dynamic control parameter

$$\Xi = \frac{k_E s_E}{r_T(d_E + S(a^*))} + \frac{k_G p_G}{r_T d_G} u(a^*)$$

exhibits dominant sensitivity to immune-kinetic parameters and promoter activation structure. Rank-based sensitivity coefficients show that variations in immune killing efficiencies $k_E$and $k_G$generate the largest shifts in Ξ, while promoter parameters $K_a$and $n_a$modulate threshold behavior and introduce nonlinear transitions consistent with bistable dynamics.

Tumor radius R affects Ξ only indirectly through its influence on equilibrium acidity a^*, indicating that Ξ remains primarily governed by reaction-kinetic and regulatory parameters rather than transport physics.

8.2 Sensitivity of the Spatial Regime (Λ)

The spatial control parameter

$$\Lambda = \sqrt{\frac{D_a}{k_U G^* R^2}}$$

is overwhelmingly dominated by physical transport quantities. Sensitivity spectra confirm that tumor radius Rexerts the strongest influence (quadratic scaling), followed by neutralization strength $k_U G^*$and proton diffusivity D_a.

Importantly, parameters associated with immune dynamics or promoter regulation produce negligible variation in Λ, demonstrating that spatial feasibility is controlled almost entirely by reaction–diffusion transport physics.

8.3 Sensitivity of the Energetic Regime (Ψ)

The energetic feasibility parameter

$$\Psi = \frac{k_U G^* a^* \eta_{\mathrm{ATP}}}{J_{\mathrm{ATP,total}}}$$

shows dominant dependence on metabolic and energetic parameters. Variations in ATP cost per proton $\eta_{ATP}$and total ATP flux $J_{ATP,total}$produce the largest sensitivity magnitudes, while tumor size influences Ψthrough volumetric scaling of proton load.

For catalytic buffering systems ($\eta_{ATP} \approx 0$), sensitivity coefficients collapse toward zero, reflecting elimination of energetic constraints and confirming that Ψrepresents a thermodynamic feasibility boundary rather than a tunable kinetic parameter.

8.4 Orthogonality of Control Axes

A central result of the sensitivity analysis is that the three parameters respond to nearly orthogonal parameter sets shown in Table 1:

Table 1. Orthogonal Control Parameters

Control Parameter	Dominant Sensitivities	Physical Domain
Ξ	k_E, k_G, K_a, n_a	Reaction kinetics / immune dynamics
Λ	$R, k_U G^*, D_a$	Transport physics

Control Parameter	Dominant Sensitivities	Physical Domain
Ψ	$\eta_{\mathrm{ATP}}, J_{\mathrm{ATP,total}}, R$	Metabolic thermodynamics

This confirms that the three bifurcations are independent and irreducible.

- No amount of immune optimization can compensate for diffusion failure.
- No amount of transport optimization can overcome ATP exhaustion.
- No amount of energetic efficiency can replace immune activation.

In summary: immune optimization cannot compensate for diffusion failure, and transport optimization cannot overcome energetic exhaustion.

8.5 Robustness of the Master Control Law

Across the full parameter sweep, the feasibility boundaries

$$\Xi > 1, \Lambda < 1, \Psi < 1$$

remained invariant. Parameter variation only moved the system within or across this feasible region; it never altered the structure of the control law itself.

Thus, the sensitivity analysis demonstrates that:

- The control law is **structurally stable**
- The phase diagram topology is parameter-robust
- Therapeutic failure modes are predictable from first principles

8.6 Interpretation

The quantitative sensitivity analysis demonstrates that tumor control behaves as a constrained physical phase system governed by three orthogonal control directions:

1. Reaction kinetics (immune control)
2. Transport physics (spatial pH reshaping)
3. Metabolic thermodynamics (energetic feasibility)

The system behaves like a constrained physical phase system.
Crossing any single feasibility boundary collapses control regardless of the remaining parameters, consistent with classical multistable nonlinear systems exhibiting independent order parameters and sharp phase transitions.

9. Experimental Predictions and Physical Falsifiability

A physical theory is defined by measurable control parameters and falsifiable phase boundaries. The three dimensionless indices introduced in Sections 3–6,

$$\Xi \text{ (dynamical clearance)}, \Lambda \text{ (spatial diffusion)}, \Psi \text{ (energetic feasibility)},$$

are constructed entirely from experimentally accessible quantities. They therefore admit direct experimental testing.

9.1 Spatial Control

$$\Lambda = \frac{1}{R}\sqrt{\frac{D}{k}},$$

where $D$is the extracellular proton diffusivity, $k$the effective neutralization rate, and $R$the tumor radius.

Reported values give:

$$D \sim 10^{-6}\text{–}10^{-5}\ \mathrm{cm^2\ s^{-1}}, \ell = \sqrt{\frac{D}{k}} \sim 50\text{–}200\ \mu\mathrm{m}, R \sim 0.5\text{–}10\ \mathrm{mm},$$

implying

$$\Lambda_{\mathrm{exp}} \sim 0.005\text{–}0.4.$$

Measured pH gradients directly fix $\ell$and thus Λ. Large tumors ($R \gtrsim 5$ mm) naturally satisfy $\Lambda \ll 1$, placing them in the diffusion-dominated regime where local alkalinization cannot globally reshape pH.

Prediction.
For $\Lambda < 1$, acidity must collapse across the tumor on the diffusion timescale

$$t_{\mathrm{diff}} \sim \frac{R^2}{D}.$$

For $R = 1$mm and $D \sim 10^{-6}\ \mathrm{cm^2/s}$, $t_{\mathrm{diff}} \sim 10^3\text{–}10^4$s (hours).

Falsifier.
Persistent pH gradients over distances $\gg \ell$ and times $\gg t_{\mathrm{diff}}$ despite estimated $\Lambda < 1$ violate the reaction–diffusion model.

9.2 Energetic Control

$$\Psi = \frac{\text{ATP demand for proton neutralization}}{\text{ATP production capacity}} \sim \frac{q\,\rho_T V}{N_c\,\Phi_{\mathrm{ATP}}/\eta},$$

where q is proton production per tumor cell, ρ_T tumor cell density, V tumor volume, N_c number of therapeutic cells, Φ_{ATP} ATP flux per cell, and η ATP cost per proton.

Typical values:

$$\Phi_{\mathrm{ATP}}^{\mathrm{bacteria}} \sim 10^6\text{–}10^7\ \mathrm{ATP/s}, \Phi_{\mathrm{ATP}}^{\mathrm{mammalian}} \sim 10^9\ \mathrm{ATP/s}, \eta \sim 1\text{–}2.$$

Thus ATP-consuming strategies possess a strict upper bound on neutralization flux.
For catalytic bicarbonate systems, $\eta \approx 0 \Rightarrow \Psi \to 0$, removing the energetic constraint.

Prediction.
ATP-dependent alkalinization must saturate as tumor size or proton load increases, producing metabolic stress, growth arrest, or collapse of pH correction.

Falsifier.
Sustained unlimited proton neutralization without metabolic penalty violates energy conservation.

9.3 Dynamical Control

$$\Xi = \frac{\text{immune killing + alkalinization-mediated suppression}}{\text{tumor growth rate}}.$$

$\Xi > 1$: tumor-free equilibrium stable, $\Xi < 1$: tumor-bearing equilibrium stable.

Prediction.
For $\Xi < 1$, tumor clearance is impossible even under perfect spatial pH control.

Falsifier.
Tumor regression while immune killing remains weaker than intrinsic growth violates the control law.

9.4 Experimental Phase Placement

Typical tumors satisfy

$$\Lambda \ll 1, \Psi \gtrsim 1$$

for substrate-dependent buffering systems, placing them beyond both spatial and energetic feasibility.
Catalytic bicarbonate strategies remove the energetic bound and are limited primarily by transport physics.

Spatial transport and energetic feasibility impose independent, irreducible bounds: diffusion limits *where* alkalinization can act, while ATP flux limits *how strongly* it can act.

9.5 Physical Interpretation

Each control axis admits direct experimental falsification:

Parameter	Measured by
Λ	spatial pH imaging
Ψ	metabolic flux measurements
Ξ	tumor regression kinetics

Tumor control is therefore feasible **if and only if**

$$\Xi > 1, \Lambda < 1, \Psi < 1.$$

This transforms alkalinization from a phenomenological strategy into a falsifiable physical control law.

9.6 Preliminary Experimental Support

While comprehensive validation of the full phase structure requires dedicated experimental studies, existing observations provide preliminary empirical consistency with key model predictions.

Spatial gradients.
Intratumoral pH imaging studies report characteristic acidity decay lengths on the order of $l \sim 100\text{–}200\ \mu m$, consistent with diffusion length scales predicted by reaction–diffusion analyses of proton transport [7]. For tumors with radii $R \sim 1\text{–}5\ mm$, this corresponds to $\Lambda = l/R \sim 0.02\text{–}0.2$, placing many macroscopic tumors near transport-limited regimes in which alkalinization cannot globally reshape tumor pH.

Energetic limits.
Observed limitations of ATP-dependent alkalinization strategies are consistent with the predicted energetic feasibility threshold $\Psi > 1$. As tumor volume increases, proton production scales volumetrically, rapidly exceeding finite metabolic power available for sustained neutralization.

Bicarbonate buffering.
Experimental studies demonstrating enhanced effects of bicarbonate-based buffering in smaller tumors but reduced efficacy in larger lesions [14] align with the model prediction that catalytic buffering mechanisms relax energetic constraints ($\Psi \to 0$) while remaining subject to spatial transport limitations.

Together, these observations are consistent with the constraint-structured control axes of the theory. Systematic experimental mapping of the full feasibility landscape defined by (Ξ, Λ, Ψ) remains an important direction for future work.

10. Discussion

The present framework treats tumor control as a constraint-structured nonlinear dynamical problem in which admissible regulatory behavior is governed by coupled dynamical, spatial, and energetic feasibility conditions. Rather than attributing outcomes to parameter magnitudes or specific mechanistic pathways, the analysis identifies dimensionless control groups (Ξ, Λ, Ψ) that define the geometry of physically realizable regulatory regimes. This formulation shifts interpretation away from mechanistic fine-tuning and toward structural properties of environmentally coupled systems, emphasizing that tumor persistence, control, and instability are governed by feasibility constraints intrinsic to the coupled dynamics.

Tumor acidity is a defining physical feature of the solid tumor microenvironment, arising from the coupled processes of proton production, diffusion, and neutralization. While acidity has long been recognized as a barrier to immune activity and therapy, its regulation has lacked a unifying quantitative framework capable of integrating nonlinear population dynamics, spatial transport, and energetic limitations. The present analysis demonstrates that tumor alkalinization is governed by a minimal set of physical constraints that jointly determine whether sustained regulatory control is feasible.

10.1 A Multi-Scale Biophysical Perspective on Alkalinization

Tumor pH regulation is controlled by three irreducible processes operating on distinct physical scales: nonlinear tumor–immune interactions, reaction–diffusion transport of protons, and metabolic energy availability. No single parameter or molecular mechanism determines outcome. Instead, tumor control requires the simultaneous satisfaction of dynamical suppression, spatial transport feasibility, and energetic sustainability. Alkalinization therefore emerges not as a purely biochemical intervention, but as a physically constrained control process governed by coupled nonlinear feedback and transport phenomena.

10.2 Spatial Constraints Outweigh Kinetic Effects in Larger Tumors

Reaction–diffusion dynamics impose a fundamental spatial constraint through the proton decay length

$$L = \sqrt{\frac{D_a}{k_U G^*}}$$

which determines whether buffering reactions can dominate diffusive proton spread. When Lexceeds the tumor radius, diffusion governs acidity structure and acidic cores persist despite strong local neutralization. This explains the enhanced susceptibility of small tumors and micrometastases to alkalinization-based strategies and the failure of spatial control in larger lesions. Crucially, this constraint is independent of promoter design, enzyme kinetics, or immune potency; unless $L < R$, global pH regulation remains physically unattainable. The resulting behavior parallels diffusion-limited regimes observed in classical reaction–diffusion systems.

10.3 Energetics as a Hard Limit on Substrate-Dependent Therapies

Energetic analysis establishes a fundamental limit on ATP-consuming alkalinization mechanisms. The maximal neutralization flux is bounded by

$$N_{H,\max} \sim \frac{J_{\mathrm{ATP,total}}}{\eta_{\mathrm{ATP}}}$$

preventing indefinite scaling of buffering capacity with tumor size or proton load. Substrate-dependent systems therefore encounter unavoidable energetic ceilings, irrespective of kinetic optimization. Catalytic bicarbonate-generating mechanisms bypass this constraint, providing a plausible explanation for their superior scalability. Energetic feasibility thus separates viable from fundamentally unsustainable regulatory strategies.

10.4 Bifurcations and Threshold Behavior in Promoter–Acidity Coupling

Promoter ultrasensitivity provides a biologically realizable mechanism for implementing sharp nonlinear thresholds within the regulatory system. Its primary dynamical consequence is the introduction of bistability and hysteresis, enabling discrete transitions between tumor-persistent and tumor-controlled states. Beyond enabling threshold-like switching behavior, promoter architecture does not modify the governing transport or energetic constraints and therefore does not alter feasibility boundaries defined by Ξ, Λ, and Ψ.

10.5 Phase Diagram Interpretation and Structural Regimes

The analytical phase diagram identifies three qualitatively distinct regimes: full control, partial (shell) control, and no control. These regimes arise from the interaction of dynamical, spatial,

and energetic feasibility constraints and are determined solely by the system's position relative to the three phase boundaries. The phase structure therefore represents a constraint-defined classification of admissible regulatory behaviors rather than a parameter-specific prediction.

10.6 Numerical Characterization of Feasibility Geometry

Numerical characterization of the feasibility space reveals that qualitative system behavior is organized by sharply defined regime boundaries aligned with the constraint inequalities. Stable tumor-controlled solutions occupy regions satisfying $\Xi > 1$, $\Lambda < 1$, and $\Psi < 1$, while violation of these constraints produces tumor persistence or instability-dominated dynamics. The emergence of well-defined regime partitions indicates that feasibility constraints act as organizing principles governing state accessibility.

Behavior near feasibility boundaries exhibits signatures characteristic of constraint-induced transitions, including prolonged transients and heightened sensitivity. Importantly, regime topology remains invariant under moderate perturbations of primitive parameters, indicating that the observed phase structure reflects intrinsic properties of the coupled nonlinear dynamics rather than numerical artifacts.

10.7 Sensitivity Analysis and Robustness of Phase Structure

Sensitivity analysis further clarifies the stability of the feasibility geometry by demonstrating that system outcomes depend predominantly on composite dimensionless groups rather than on individual kinetic parameters. Variations in primitive parameters influence behavior primarily through their effects on Ξ, Λ, and Ψ. The persistence of regime topology under parameter variation supports the interpretation of feasibility boundaries as structural features of the system's dynamical organization.

10.8 Phase Structure of Tumor Control

Tumor clearance emerges from the simultaneous satisfaction of three independent physical constraints: dynamical dominance of suppression over growth, spatial dominance of neutralization over diffusion, and energetic sustainability of buffering. These constraints are encoded by the control parameters Ξ, Λ, and Ψ, each arising from distinct physical principles. None can compensate for failure of the others. Immune potency cannot overcome diffusion-dominated acidity, efficient transport cannot bypass energetic exhaustion, and energetic efficiency cannot replace dynamical suppression.

In this formulation, the tumor microenvironment behaves as a coupled reaction–diffusion–energy system whose phase structure governs regulatory outcomes. Cancer therapy is thus recast from a problem of biological optimization into one of physical control — identifying and crossing feasibility boundaries separating tumor persistence from admissible control regimes.

10.9 Novelty and Conceptual Contribution

The principal contribution of this study is conceptual rather than mechanistic. Instead of proposing new biochemical pathways or kinetic refinements, the framework establishes a unified feasibility-based description linking nonlinear dynamics, reaction–diffusion transport, and metabolic energetics within a single constraint geometry. This abstraction clarifies why regulatory success or failure may arise independently of biological detail and provides a generalizable perspective for analyzing environmentally coupled regulatory systems.

11. Conclusion

Tumor control emerges as a constrained physical problem rather than a purely biological one. The analysis demonstrates that regulatory success is governed by irreducible limits imposed by nonlinear dynamics, reaction–diffusion transport, chemical buffering, and energetic feasibility. Tumor elimination is therefore admissible only when dynamical suppression overcomes intrinsic growth, spatial transport permits reshaping of acidity gradients, and metabolic power sustains alkalinization. Improvements in immune potency, molecular targeting, or genetic circuit design cannot compensate for violations of these underlying constraints.

These results are formalized in the Biophysical Feasibility Theorem for Tumor Control, which establishes that tumor clearance is possible if and only if three independent and orthogonal feasibility conditions are simultaneously satisfied:

$$\Xi > 1, \Lambda < 1, \Psi < 1.$$

Here, Ξ defines a dynamical transition separating suppression-dominated and growth-dominated regimes, Λ defines a transport-controlled boundary governing spatial pH regulation, and Ψ defines an energetic constraint imposed by finite metabolic resources. Together, these inequalities define a sharply bounded admissible region in feasibility space representing a necessary-and-sufficient condition for sustained tumor control.

Numerical characterization of the feasibility space reveals that qualitative system behavior is organized by sharply defined regime boundaries aligned with the constraint inequalities. Stable tumor-controlled states occupy regions satisfying $\Xi > 1$, $\Lambda < 1$, and $\Psi < 1$, while violation of these conditions produces tumor persistence or instability-dominated dynamics. Sensitivity analysis further demonstrates that regime topology remains robust under moderate parameter perturbations, indicating that the feasibility boundaries represent intrinsic structural features of the coupled dynamics rather than artifacts of parameterization. These findings collectively support the interpretation of tumor regulation as a constraint-structured nonlinear phenomenon governed by feasibility geometry.

The principal novelty of this study lies in the formulation of tumor control as a feasibility-constrained dynamical system rather than as a parameter-optimized biological process. Instead of introducing new kinetic interactions or biochemical mechanisms, the framework identifies dimensionless control groups that define the geometry of physically realizable regulatory

regimes. This abstraction clarifies why therapeutic success or failure may arise independently of biological detail and provides a generalizable constraint-based description linking nonlinear dynamics, transport physics, and metabolic energetics within a unified control structure.

The resulting control law,

$$\text{Control} = f(\text{dynamics},\text{transport},\text{energetics}),$$

expresses tumor regulation as a problem of dynamical admissibility governed by constraint satisfaction rather than by isolated mechanistic enhancement. No single intervention strategy — immune activation, buffering chemistry, or genetic circuit design — guarantees tumor elimination in isolation.

11.1 Generality: Beyond Tumor Systems

Although derived for tumor–immune–acidity dynamics, the Biophysical Feasibility Theorem expresses a constraint structure that is not necessarily specific to tumors. The feasibility parameters (Ξ, Λ, Ψ) arise from generic physical principles — nonlinear regulatory interactions, reaction–diffusion transport, and finite energetic resources — which govern a broad class of environmentally coupled living systems.

Systems in which organisms modify their local environment, where environmental modification feeds back onto population viability, and where both processes are limited by diffusion and energetic costs naturally exhibit analogous feasibility boundaries. Examples include microbial ecosystems generating inhibitory metabolite gradients, biofilm communities constrained by diffusion-limited transport, and synthetic regulatory circuits operating under metabolic resource limitations.

In such systems, qualitative regime transitions are likewise governed by the relative dominance of interaction dynamics, transport processes, and energetic sustainability. The specific biological mechanisms vary, but the constraint-defined phase structure remains invariant. Tumor systems therefore represent one realization of a more general class of feasibility-limited regulatory dynamics.

12. Declarations

Funding: No funding was received for conducting this study.

Clinical trial number: Not applicable.

Ethics approval, consent to participate, and consent to publish: Not applicable. This theoretical model paper does not involve human participants, animal experiments, or clinical data.

Conflict of interest: The authors declare that they have no conflicts of interest.

13. Data and Code Availability

All computational models, simulation code, and analysis scripts are publicly available at URL: https://github.com/erosarioaloma/feasibility-constraints-nonlinear-systems.git

The data is archived at Zenodo: DOI: 10.5281/zenodo.18675107, available at URL: https://zenodo.org/records/18675107

14. Author Contributions Statement

Enrique Rosario Aloma – Senior scientist on the project. Conceived the study, developed the methodological framework, and carried out the mathematical modeling, simulations, statistical analyses, and data collection. Drafted final draft of the manuscript.

Luis Rodriguez – organized the study data and worked on the initial manuscript draft. Contributed to the organization, editing, and revision of the article to ensure clarity, cohesion, and logical structure.

Carolina Vigo – assisted in reviewing statistical analysis and simulation data. Prepared files for repository deposit. Reviewed first draft.

Maymunah Ray - Assisted in reviewing mathematical modeling and collection of data. Assisted in building the first draft.

Rolando Petit – Assisted building figures and reviewed all citations, references, figures, and tables to ensure accuracy, clarity, and compliance with ethical publishing standards. Assisted drafting final draft.

15. References

- Estrella, V. et al. Acidity generated by the tumor microenvironment drives local invasion. *Cancer Res.* **73**, 1524□1535 (2013).
- Webb, B.A., Chimenti, M., Jacobson, M.P. & Barber, D.L. Dysregulated pH: a perfect storm for cancer progression. *Nat. Rev. Cancer* **11**, 671□677 (2011).
- Parks, S.K., Chiche, J. & Pouyss⌈gur, J. pH control mechanisms of tumor survival and growth. *J. Cell Physiol.* **226**, 299□308 (2011).
- Gatenby, R.A. & Gillies, R.J. Why do cancers have high aerobic glycolysis? *Nat. Rev. Cancer* **4**, 891□899 (2004).

- Martin, N.K. et al. A mathematical model of tumour acidity: Implications for cancer therapy. *Math. Biosci.* **277**, 1□15 (2016).
- Smallbone, K., Gavaghan, D.J., Gatenby, R.A. & Maini, P.K. The role of acidity in solid tumour growth and invasion. *J. Theor. Biol.* **235**, 476□484 (2005).
- Helmlinger, G., Yuan, F., Dellian, M. & Jain, R.K. Interstitial pH gradients in solid tumors in vivo. *Nat. Med.* **3**, 177□182 (1997).
- Griffiths, J.R. Are cancer cells acidic? *Br. J. Cancer* **64**, 425□427 (1991).
- Fischer, K. et al. Inhibitory effect of tumor cell-derived lactic acid on human T cells. *Blood* **109**, 3812□3819 (2007).
- Calcinotto, A. et al. Modulation of microenvironment acidity reverses T-cell anergy. *Cancer Res.* **72**, 2746□2756 (2012).
- Brand, A. et al. LDHA-associated lactic acid production blunts tumor immunosurveillance. *Cell Metab.* **24**, 657□671 (2016).
- Hill, A.V. The possible effects of molecular aggregation of haemoglobin. *J. Physiol.* **40**, iv□vii (1910).
- Gatenby, R.A. et al. Cellular adaptations to hypoxia and acidosis. *Br. J. Cancer* **97**, 646□653 (2007).
- Robey, I.F. et al. Bicarbonate increases tumor pH and inhibits metastases. *Cancer Res.* **69**, 2260□2268 (2009).
- Ibrahim-Hashim, A. et al. Systemic buffers inhibit carcinogenesis. *J. Urol.* **188**, 624□631 (2012).
- Xie, J. et al. Tumor acidity triggers drug resistance niches. *Sci. Adv.* **4**, eaat1602 (2018).
- Russell, J.B. & Cook, G.M. Energetics of bacterial growth. *Microbiol. Rev.* **59**, 48□62 (1995).
- Kuznetsov, V.A., Makalkin, I.A., Taylor, M.A. & Perelson, A.S. Nonlinear dynamics of immunogenic tumors. *Bull. Math. Biol.* **56**, 295□321 (1994).
- Kirschner, D. & Panetta, J.C. Modeling immunotherapy of tumor□immune interactions. *J. Math. Biol.* **37**, 235□252 (1998).
- de Pillis, L.G., Radunskaya, A.E. & Wiseman, C.L. A validated mathematical model of immune response to tumor growth. *Cancer Res.* **65**, 7950□7958 (2005).

- Anderson, A.R.A. & Chaplain, M.A.J. Continuous and discrete models of tumor-induced angiogenesis. *Bull. Math. Biol.* **60**, 857□899 (1998).
- Turing, A.M. The chemical basis of morphogenesis. *Phil. Trans. R. Soc. B* **237**, 37□72 (1952).
- Murray, J.D. *Mathematical Biology I.* Springer (2002).
- Murray, J.D. *Mathematical Biology II.* Springer (2003).
- Nelson, P. *Biological Physics.* W.H. Freeman (2004).
- LeVeque, R.J. *Finite Difference Methods.* SIAM (2007).
- Hairer, E., N⁄rsett, S.P. & Wanner, G. *Solving ODEs I.* Springer (1993).
- Gardner, T.S., Cantor, C.R. & Collins, J.J. Construction of a genetic toggle switch. *Nature* **403**, 339□342 (2000).
- Elowitz, M.B. & Leibler, S. A synthetic oscillatory network. *Nature* **403**, 335□338 (2000).
- Kuznetsov, Y.A. *Elements of Applied Bifurcation Theory.* Springer (2004).
- Strogatz, S.H. *Nonlinear Dynamics and Chaos.* Westview Press (2015).
- Wiggins, S. *Introduction to Applied Nonlinear Dynamical Systems.* Springer (2003).

Supplementary Files

This is a list of supplementary files associated with this preprint. Click to download.

- GraphicalAbstract.jpeg